

# Molecular packing-dependent exciton dynamics in functionalized anthradithiophene derivatives: From solutions to crystals F

Cite as: J. Chem. Phys. **153**, 164715 (2020); <https://doi.org/10.1063/5.0026072>

Submitted: 20 August 2020 . Accepted: 05 October 2020 . Published Online: 29 October 2020

J. D. B. Van Schenck, G. Mayonado, J. E. Anthony , M. W. Graham , and O. Ostroverkhova 

## COLLECTIONS

Note: This paper is part of the JCP Special Topic on Up- and Down-Conversion in Molecules and Materials.

F This paper was selected as Featured



View Online



Export Citation



CrossMark



Meet the Next Generation  
of Quantum Analyzers

And Join the Launch  
Event on November 17th



Register now



Zurich  
Instruments

# Molecular packing-dependent exciton dynamics in functionalized anthradithiophene derivatives: From solutions to crystals

Cite as: J. Chem. Phys. 153, 164715 (2020); doi: 10.1063/5.0026072

Submitted: 20 August 2020 • Accepted: 5 October 2020 •

Published Online: 29 October 2020



View Online



Export Citation



CrossMark

J. D. B. Van Schenck,<sup>1</sup> G. Mayonado,<sup>1</sup> J. E. Anthony,<sup>2</sup>  M. W. Graham,<sup>1</sup>  and O. Ostroverkhova<sup>1,a)</sup> 

## AFFILIATIONS

<sup>1</sup>Department of Physics, Oregon State University, Corvallis, Oregon 97330, USA

<sup>2</sup>Department of Chemistry, University of Kentucky, Lexington, Kentucky 40506, USA

**Note:** This paper is part of the JCP Special Topic on Up- and Down-Conversion in Molecules and Materials.

**a) Author to whom correspondence should be addressed:** [oksana@science.oregonstate.edu](mailto:oksana@science.oregonstate.edu)

## ABSTRACT

Understanding the impact of inter-molecular orientation on the optical properties of organic semiconductors is important for designing next-generation organic (opto)electronic and photonic devices. However, fundamental aspects of how various features of molecular packing in crystalline systems determine the nature and dynamics of excitons have been a subject of debate. Toward this end, we present a systematic study of how various molecular crystal packing motifs affect the optical properties of a class of high-performance organic semiconductors: functionalized derivatives of fluorinated anthradithiophene. The absorptive and emissive species present in three such derivatives (exhibiting “brickwork,” “twisted-columnar,” and “sandwich-herringbone” motifs, controlled by the side group R) were analyzed both in solution and in single crystals, using various modalities of optical and photoluminescence spectroscopy, revealing the nature of these excited states. In solution, in the emission band, two states were identified: a Franck–Condon state present at all concentrations and an excimer that emerged at higher concentrations. In single crystal systems, together with *ab initio* calculations, it was found in the absorptive band that Frenkel and Charge Transfer (CT) excitons mixed due to nonvanishing CT integrals in all derivatives, but the amount of admixture and exciton delocalization depended on the packing, with the “sandwich-herringbone” packing motif least conducive to delocalization. Three emissive species in the crystal phase were also identified: Frenkel excitons, entangled triplet pairs <sup>1</sup>(TT) (which are precursors to forming free triplet states via singlet fission), and self-trapped excitons (STEs, similar in origin to excimers present in concentrated solution). The “twisted-columnar” packing motif was most conducive to the formation of Frenkel excitons delocalized over 4–7 molecules depending on the temperature. These delocalized Frenkel states were dominant across the full temperature range (78 K–293 K), though at lower temperatures, the entangled triplet states and STEs were present. In the derivative with the “brickwork” packing, all three emissive species were observed across the full temperature range and, most notably, the <sup>1</sup>(TT) state was present at room temperature. Finally, the derivative with the “sandwich-herringbone” packing exhibited localized Frenkel excitons and had a strong propensity for self-trapped exciton formation even at higher temperatures. In this derivative, no formation of the <sup>1</sup>(TT) state was observed. The temperature-dependent dynamics of these emissive states are reported, as well as their origin in fundamental inter-molecular interactions.

Published under license by AIP Publishing. <https://doi.org/10.1063/5.0026072>

## I. INTRODUCTION

Organic semiconductors are of interest due to their applications in low-cost, large-area (opto)electronic and photonic devices; these include thin-film transistors (TFTs), solar cells, light-emitting diodes, photodetectors, sensors, and many others.<sup>1</sup> Tremendous

progress in device performance has been achieved over the past 10 years due to a better understanding of the fundamental processes that determine (opto)electronic properties of organic materials, as well as the structure–property relations that led to the development of improved fabrication methods, enabling optimized film structure and morphology. Despite the progress, many fundamental questions

pertaining to the photophysics of organic materials, especially crystalline materials, remain. These include those related to the nature of excitons,<sup>2–4</sup> the underlying interactions<sup>5,6</sup> and delocalization,<sup>7</sup> and how these properties contribute to processes such as singlet fission<sup>8</sup> and charge photogeneration.<sup>9,10</sup> For studies of these fundamental properties, organic systems with long-range order such as molecular crystals are especially valuable.<sup>6,11–18</sup> For the molecular design of next-generation organic optical materials, it is also important to understand how exciton properties evolve depending on the molecular structure and packing. Toward this goal, we present a comprehensive investigation of the exciton nature and properties in fluorinated anthradithiophene (diF R-ADT) crystals functionalized with various side groups (R) that determine molecular packing.

Organic crystals of various acene derivatives (e.g., tetracene, pentacene, and rubrene) have served as model systems for a variety of studies of exciton dynamics.<sup>4,17,19</sup> The contributions of the vibronically coupled Frenkel excitons and charge transfer (CT) excitons to the absorption spectra as well as the implications of the Frenkel-CT exciton admixture for exciton dissociation, diffusion, and singlet fission have been vigorously debated.<sup>3,17,18,20,21</sup> Interpretation is often complicated due to the many and diverse kinds of interactions that include both short-range interactions mediated by a direct wavefunction overlap (which are highly sensitive to the molecular orientations and can constructively or destructively interfere depending on the sign of the transfer integral) and long-range

Coulomb-mediated interactions.<sup>2</sup> The photophysical picture is further confounded by processes such as singlet fission<sup>13,22,23</sup> and by the existence and interplay of electronic states with different properties (including localized and delocalized Frenkel excitons, Davydov pairs, delocalized CT excitons, and excimers) in organic crystalline systems.<sup>24,25</sup>

Contributions of molecular packing to various aspects of exciton dynamics in organic crystals have also been under investigation. For example, in pentacene (Pn) polymorphs, the Davydov splitting as well as the energies and oscillator strengths of the higher-lying energy states were found to be considerably more sensitive to the polymorph structure than the energy of the lowest excited state.<sup>21</sup> In perylene crystals, the  $\alpha$ - and  $\beta$ -phases characterized by different molecular packing exhibited considerably different exciton delocalization properties.<sup>26</sup> These were related to differences in the extent of the exciton band dispersion, which manifested in dramatically different photoluminescence (PL) lifetimes.<sup>26</sup> In functionalized anthracene crystals, the formation of excimers was found to be highly dependent on the molecular packing.<sup>27</sup>

In the present study, we investigated how molecular packing determines various aspects of the photophysics in crystals of three functionalized anthradithiophene (ADT) derivatives: diF TES-ADT [TES = (triethylsilyl)ethynyl], diF TSBS-ADT (TSBS = tri-*sec*-butylsilylethynyl), and diF TBDMS-ADT (TBDMS = tert-butyltrimethylsilylethynyl) (Fig. 1). Functionalized fluorinated ADT

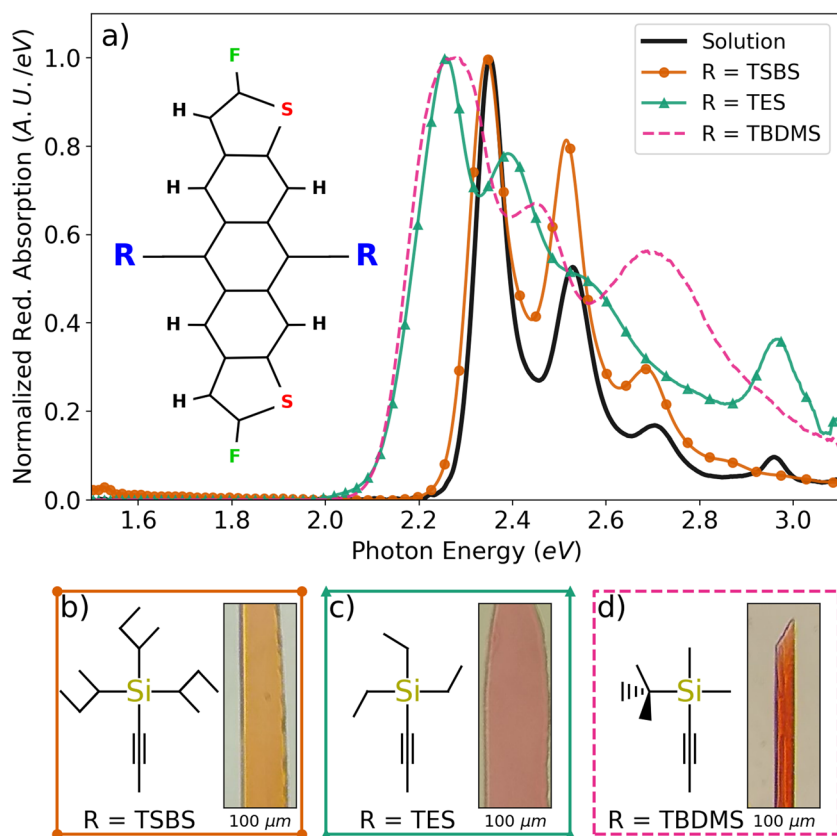


**FIG. 1.** (a) The normalized reduced absorption of diF R-ADT in solution (R = TES, 30  $\mu$ M in chlorobenzene; solid line; see the [supplementary material](#) for R = TSBS and TBDMS) and in the crystal phase [R = TSBS (dots), TES (triangles), and TBDMS (dashed line)], polarized so as to maximize the absorption. The inset shows the chemical structure for diF R-ADT (in the *syn*-ADT configuration, see Fig. S2). [(b)–(d)] Chemical structures for the three side groups: R = TSBS, TES, and TBDMS. Insets show a representative microscope image of each crystal with scale bar at the bottom indicating the width of the image.

derivatives have been extensively studied<sup>1</sup> in field-effect transistors (FETs) (both in the single-crystal and in the thin-film form) and in devices relying on the ADT's strong photoconductive response<sup>1</sup> and singlet fission.<sup>28</sup> For example, the diF TES-ADT derivative exhibited hole mobilities of up to  $\sim 20$  cm<sup>2</sup>/(V s) in pristine crystalline films<sup>29</sup> and up to  $\sim 7$  cm<sup>2</sup>/(V s) in ultra-thin highly ordered diF TES-ADT:PS (PS = polystyrene) films.<sup>30</sup> Most recently,<sup>31</sup> strong exciton-photon coupling, with a Rabi splitting of 340 meV, was observed in diF TES-ADT:PMMA polycrystalline films in all-metal microcavities. This makes diF R-ADT derivatives potentially attractive not only for traditional (opto)electronic applications but also for applications relying on the properties of exciton polaritons.<sup>32–34</sup> Some aspects of the photophysics of diF TES-ADT have been previously studied in polycrystalline thin films<sup>28,35–37</sup> and in blends with polymers and other small molecules.<sup>38,39</sup> However, the photophysics of single crystals offers a considerably deeper insight into fundamental properties of excitons, which has not been previously reported for diF R-ADT. Here, we present a comprehensive study of exciton dynamics in diF TES-ADT, diF TSBS-ADT, and diF TBDMS-ADT crystals chosen due to their similar molecular properties but drastically different packing motifs. Using polarization-dependent optical absorption and temperature-dependent time-resolved PL spectroscopy, combined with density functional theory (DFT), we establish how features in the exciton nature and dynamics are determined by various aspects of the crystal structure.

## II. MATERIALS AND METHODS

### A. Materials

The choice of the diF R-ADT derivatives with R = TES, TSBS, and TBDMS (Fig. 1) was motivated by the following considerations: (1) the crystal structures of all three derivatives have been established in previous studies, and methods of crystal growth from solutions were developed; (2) their distinctly different packing motifs are expected to exhibit a range of behaviors for the exciton nature and properties; and (3) all three derivatives have been studied in electronic devices,<sup>40–44</sup> thus providing opportunities to probe deeper connections between exciton and charge carrier dynamics. In particular:

- (i) The diF TES-ADT derivative exhibits a two-dimensional (2D) “brickwork” molecular packing [Figs. 2(a) and 2(b)], one of the most successful packing motifs for FETs. The diF TES-ADT single crystal has a triclinic structure with one molecule per unit cell ( $Z = 1$ ) and unit cell parameters  $a = 7.21$  Å (7.12 Å),  $b = 7.32$  Å (7.23 Å),  $c = 16.35$  Å (16.63 Å),  $\alpha = 87.72^\circ$  (97.52°),  $\beta = 89.99^\circ$  (91.36°), and  $\gamma = 71.94^\circ$  (107.49°) at temperatures above (below) 294 K, with a solid–solid phase transition occurring at 294 K.<sup>40</sup> The “brickwork” packing structure of diF TES-ADT exists in the  $a$ – $b$  plane such that the molecular backbones are  $\pi$ -stacked in a 2D sheet [Fig. 2(a)]; in the  $c$ -direction, these 2D sheets are well separated by  $\sim 16$  Å [Fig. 2(b)], which minimizes inter-sheet interactions. Each molecule in the 2D sheets has six neighbors, though only four have a short  $\pi$ – $\pi$  stacking distance [ $\sim 3.5$  Å, e.g., pairs 1–2 and 1–4 and their inversion-symmetric pairs in Fig. 2(a)] and a significant

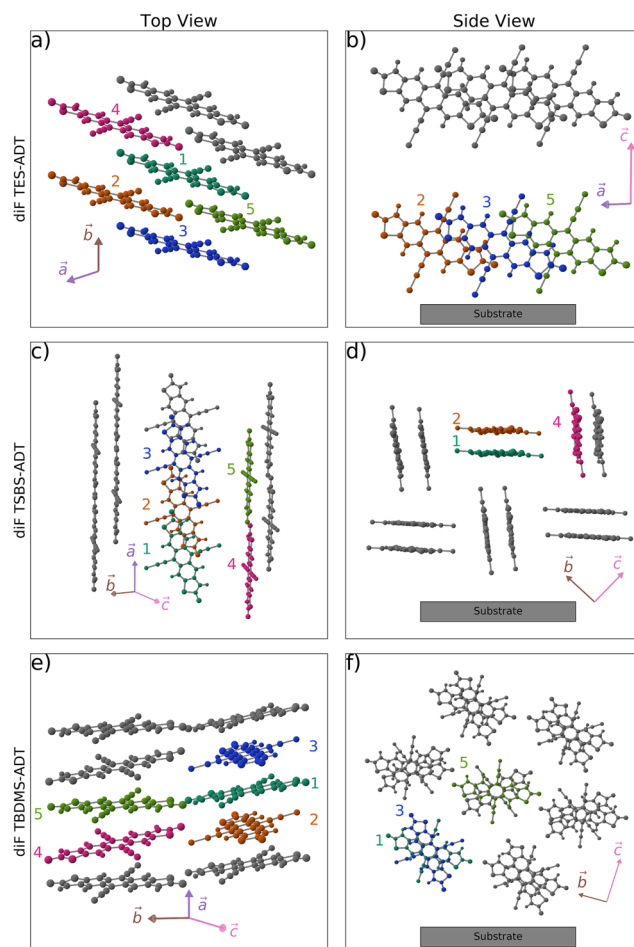


**FIG. 2.** The crystalline structures of diF R-ADT (R = TES, TSBS, and TBDMS). [(a), (c), and (e)] Top view of the crystal when grown on a glass substrate with the vertical orientation corresponding to the fast growth direction (i.e., “long axis” of the crystal). [(b), (d), and (f)] Side view of the crystal, viewed along the fast growth direction (i.e., “long axis” of the crystal, with the substrate shown). Each pair of figures has selected molecules indexed for reference in the main text. In all figures, the side groups are omitted and only the *syn*-ADT isomer is shown for clarity. For diF TES-ADT, the low temperature ( $T < 294$  K) crystal phase is shown.

overlap of molecular orbitals. Crystals grown from solution on a glass substrate exhibit (00 $l$ ) orientation ( $l = 1, 2, 3, 4$ ) (Fig. S1) so that the 2D sheet is parallel to the plane of the substrate,<sup>41</sup> with the  $b$ -axis as the fast growth axis identified in previous studies.<sup>45</sup>

- (ii) The diF TSBS-ADT derivative exhibits a 1D “sandwich-herringbone” packing motif [Figs. 2(c) and 2(d)]. The diF TSBS-ADT single crystal has a triclinic structure with  $Z = 4$  and unit cell parameters  $a = 15.07$  Å,  $b = 16.45$  Å,  $c = 18.25$  Å,  $\alpha = 90^\circ$ ,  $\beta = 103.06^\circ$ , and  $\gamma = 90^\circ$ .

The “sandwich-herringbone” packing structure of diF TSBS-ADT exists along the  $a$ - and  $b/c$ -axes. In particular,

along the  $a$ -axis is the “sandwich” structure [Fig. 2(c)], where pairs of molecules with approximate glide reflection symmetry form a 1D chain (similar to the pattern footsteps make—where each “print” is offset forward and laterally from the previous “print”). The pairs of inequivalent molecules in these chains are  $\pi$ -stacked, with a large slip distance between pairs (so that the slip distance constitutes about 50% of the molecular backbone length), and so, each molecule has only two nearest neighbors [e.g., for molecule 2, pairs 1–2 and 2–3 in Fig. 2(c)]. In the  $b$ - $c$  plane [Fig. 2(d)], these chains form a herringbone pattern with a  $90^\circ$  rotation between the molecular backbones in inequivalent chains. Each chain is separated from its inequivalent neighbors [four in total, exemplified by pair 2–4 in Fig. 2(d)] by  $\sim 11$  Å, making the inter-chain excited-state interactions far longer-ranged than the intra-chain excited-state interactions. When grown from solution on a glass substrate, diF TSBS-ADT crystals exhibit a  $(0ll)$  ( $l = 1, 2, 3$ ) orientation (Fig. S1), with the  $a$ -axis as the fast growth axis.<sup>41</sup>

- (iii) The diF TBDMS-ADT derivative exhibits a 1D “twisted columnar” packing motif [Figs. 2(e) and 2(f)]. The diF TBDMS-ADT single crystal has a monoclinic structure with  $Z = 4$  and unit cell parameters  $a = 7.92$  Å,  $b = 15.37$  Å,  $c = 26.68$  Å,  $\alpha = 90^\circ$ ,  $\beta = 97.04^\circ$ , and  $\gamma = 90^\circ$ .

The “twisted columnar” packing structure of diF TBDMS-ADT exists along the  $a$ -axis. Adjacent molecules are  $\pi$ -stacked (with the  $\pi$ - $\pi$  distance of 3.6 Å), with a small ( $\sim 10\%$  of molecular backbone length) slip distance between pairs exemplified by the 1–2 pair in Fig. 2(e). So, the molecules form a pattern similar to a “leaning column,” which we hereafter refer to as a “column” to differentiate it from the “footstep-patterned 1D chain” of diF TSBS-ADT crystals [cf. Figs. 2(c) and 2(e)]. Additionally, there is an  $\sim 45^\circ$  intra-column rotational offset between adjacent molecular backbones [see pairs 1–3 or 4–5 in Figs. 2(e) and 2(f)]. In the  $b$ - $c$  plane, the columns are well separated from each other [with an inter-column distance of  $\sim 16$  Å, exemplified by pair 1–5 in Fig. 2(e)]. When grown from solution onto a glass substrate, the crystals exhibit a  $(0lm)$  ( $l = 1, 2$  and  $m = 2, 4$ ) orientation on the substrate (Fig. S1) with the  $a$ -axis as the fast growth axis identified in previous studies.<sup>43</sup>

All diF R-ADT derivatives under study contained a 35:65 mixture of *syn*- and *anti*-isomers of diF R-ADT defined with respect to the Sulfur atom positions on the molecular backbone.<sup>46</sup> For simplicity, figures showing molecular structures (e.g., Figs. 1 and 2) include only the *syn*-ADT isomer. Molecular structure and pertinent properties of the *syn*- and *anti*-ADT isomers are included in the [supplementary material](#) (Figs. S2 and S3 and Table SIII).

## B. Sample preparation

For studies related to the concentration dependence of diF R-ADT spectral features in solution, molecules were dissolved in chlorobenzene at concentrations ranging from  $5 \mu\text{M}$  to  $0.2$  M. Single crystals of diF R-ADT ( $R = \text{TSBS, TES, and TBDMS}$ ) were prepared by drop casting from chlorobenzene solutions at concentrations ranging between  $1$  mM and  $5$  mM.  $20 \mu\text{L}$  drops of solution were placed onto glass substrates. The substrates were then covered

and kept in a  $0^\circ\text{C}$  environment to slow the evaporation process to several hours. This procedure resulted in the formation of high aspect ratio ( $\sim 100$ ) platelet-like crystals with short dimensions typically ranging between  $10 \mu\text{m}$  and  $100 \mu\text{m}$  [Figs. 1(b)–1(d)] due to anisotropic growth rates along each of the in-plane crystal axes. The “short” and “long” sides of these platelets will be referred to as “short axis” and “long axis” of the crystals—where the “long axis” corresponds with the fast growth direction. Crystal thicknesses varied between  $200$  nm and  $1 \mu\text{m}$ , estimated on the microscope by focusing light onto two faces of the crystal. Only crystals that were confirmed to have only a single domain under crossed polarizers were selected for our studies. Measurements were done on at least three crystals of each derivative.

## C. Measurements of optical absorption

In solution, optical absorption was measured in a  $1$  cm fused silica cuvette using a fiber-coupled tungsten white light source and an Ocean Optics USB 2000 spectrometer.

Polarization-resolved optical absorption from crystals was measured in a transmissive geometry using a modified inverted confocal microscope (Olympus IX-71). Collimated white light was passed through a linear polarizer and focused onto the sample with a spot diameter of  $30 \mu\text{m}$ . Transmitted light was collected with a  $10\times$  objective and then analyzed with an Ocean Optics USB 2000 spectrometer. For polarization-dependent measurements, the polarizer was rotated in steps of  $10^\circ$ . All polarizations are referenced with respect to the “long axis” (i.e., fast growth direction) of the crystal defined above.

In order to assess the “out-of-plane” absorption characteristics, the sample was tilted at angles between  $0^\circ$  and  $60^\circ$  (so that the plane of incidence contained the substrate normal and either the “long” or “short” crystal axis) and absorption was measured via p-polarized multiple-angle incidence resolution spectrometry (pMAIRS).<sup>47</sup>

Absorption spectra were all fit as “reduced absorption,” that is, the absorbance divided by the photon energy, which corrects for the linear dependence of absorption on photon energy [cf. Eq. (S1)]; details on fits are discussed in the [supplementary material](#).

## D. Measurements of photoluminescence

The steady-state photoluminescence (PL) for all samples was measured using  $355$  nm laser (44 kHz Q-switched frequency-tripled pulsed Nd:YAG laser, Nanolase, Inc.) excitation. In solution, the excitation beam was collimated and the PL was collected off-axis with a parabolic mirror, as detailed in our previous work.<sup>36</sup> For measurements in crystals, samples were placed on an inverted microscope, the laser excitation was focused onto the sample through a  $10\times$  objective, and PL was collected in reflection through that same objective and analyzed with the Ocean Optics USB2000-FLG spectrometer. Selected samples were also excited at  $532$  nm (frequency-doubled Nd:YVO<sub>4</sub> continuous wave laser, Verdi-5, Coherent, Inc.) to confirm that the PL line shapes were not dependent upon excitation wavelength. All PL spectra were fit as “reduced PL,” that is, the PL counts divided by the photon energy cubed, which corrects for the cubic dependence of spontaneous emission on photon energy [cf. Eq. (S2)]. Details on fits are discussed in the [supplementary material](#).

To quantify the wavelength-dependent PL kinetics of diF R-ADT crystals and solutions, we employed Time Correlated Single Photon Counting (TCSPC). A 532 nm pulsed laser (500 kHz frequency-doubled Nd:YAG laser, Fianium HE-1060) was used to excite the samples using the geometries described above. The collected PL emission was filtered using a 532 nm long-pass filter and analyzed using a fiber-coupled monochromator [Newport/Oriel, full width at half maximum (FWHM) = 10 nm] and avalanche photo diode (APD, Molecular Photonic Devices) assembly custom built for TCSPC. The APD signal was analyzed with a TimeHarp 200 card (PicoQuant, Inc.). The Instrument Response Function (IRF) was measured by scattering attenuated excitation light (pristine solvent or substrate, depending on the measurement type) through the setup with the 532 nm long-pass filter removed from the detection path. This yielded a pulse FWHM of  $\sim 270$  ps. The PL time traces were fit assuming a multiexponential decay convoluted with the IRF as follows:

$$I(t) = \left\{ IRF(t) * \sum_i \beta_i k_i \exp(-k_i t) \right\} + BG.$$

Here,  $I(t)$  is the normalized PL,  $k_i$  and  $\beta_i$  are the decay rates and weight factors for each component,  $IRF(t)$  is the normalized IRF, and  $BG$  is the time-independent background noise. All parameter values were extracted from experimental fits using Maximum Likelihood Estimation (MLE), as described in the [supplementary material](#).<sup>48,49</sup> All temperature-dependent PL measurements in crystals were obtained by placing a sample in a Janis Research ST-500-UC cryostat cooled with liquid nitrogen, which was mounted on an Olympus IX-71 inverted microscope.

### E. Density functional theory

To assess the excited state properties of isolated diF R-ADT (R = TSBS, TES, and TBDMS) molecules (monomers), Time-Dependent Density Functional Theory (TD-DFT) methods were employed. First, the initial geometries of these molecules were optimized using DFT methods with the B3LYP functional and the 6-31G(d, p) basis set. Energies, oscillator strengths, and transition dipole moments (TDMs) of the first four excited states were then calculated using TD-DFT at the same level of theory. Previous studies of ADT and Pn derivatives,<sup>36,50</sup> as well as our experimental optical absorption data in dilute solution (see Fig. S4), demonstrate that varying the molecular side group (R = TSBS, TES, and TBDMS) has a negligible impact on lowest-energy excited states since the exciton wavefunction is located primarily on the ADT backbone and does not extend past the Si atoms on the side groups. So, to reduce computational complexity, all subsequent calculations were done with the reduced side group R = SiH<sub>3</sub>. See Figs. S2 and S3 and Table SIII provided in the [supplementary material](#).

The intermolecular interactions in each diF R-ADT crystal were assessed using TD-DFT methods at the same level of theory. For each crystalline system (R = TES, TSBS, and TBDMS), the nearest neighbor intermolecular distances and orientations were extracted from the crystal structures experimentally obtained from XRD measurements. These distances and orientations were used together with the optimized diF SiH<sub>3</sub>-ADT monomer geometry to construct all nearest neighbor dimer pairs (indexed in Fig. 2). The

orbital energies for each dimer system were calculated with DFT, and the excited state energies, oscillator strengths, and TDMs were calculated for the first six excited states with TD-DFT. To aid the qualitative description of each excited-state transition, the Natural Transition Orbitals (NTOs)<sup>51</sup> were calculated for each transition. The magnitude of the electron and hole hopping integrals ( $t_e$  and  $t_h$ ) were evaluated via the energy splitting method,<sup>2</sup> and the magnitude of the resonant intermolecular coupling ( $V$ ) was similarly estimated from the energy splitting of the dimer excited-state energies, as detailed in the [supplementary material](#). All calculations were carried out with the Gaussian16 software suite,<sup>52</sup> with *syn*-ADT molecular backbones (unless otherwise stated) to simplify the qualitative assignments of TDMs and excited states to underlying physical phenomena.

## III. RESULTS

### A. Optical properties of solutions

In order to understand how specific aspects of molecular packing in the solid phase affect the optical properties, we first studied in detail properties of diF R-ADT molecules in solution, at various concentrations.

Figures 1(a) and S4 show the optical absorption spectrum of diF R-ADT in a 30  $\mu$ M chlorobenzene solution, while Fig. 3(a) shows PL spectra of diF TES-ADT in solution at concentrations ranging between 350  $\mu$ M and 0.14M. In all three diF R-ADT derivatives under study (R = TES, TSBS, and TBDMS), optical absorption spectra of dilute (<100  $\mu$ M) solutions were well described using a Frank-Condon (FC) vibronic progression<sup>1,2,53,54</sup> [Eq. (S1)] with the homogeneously broadened 0-0 resonance at 2.355 eV (FWHM = 0.065 eV), followed by 0-n (n = 1, 2, 3) vibronic replica peaks at 0.175 eV intervals due to the exciton coupling to a C-C stretch mode of the diF R-ADT backbone with the Huang-Rhys factor of 0.69 (Fig. S5).<sup>54</sup> Identical properties of diF R-ADT in dilute solution (Fig. S4) indicate that the side groups have a negligible influence on the optical properties of the isolated molecules, in agreement with previous studies of various ADT and Pn derivatives.<sup>36,55,56</sup> All derivatives exhibited an  $\sim 10$  nm Stokes shift, consistent with a rigid structure of the ADT backbone, and so, the steady-state PL spectra from dilute solutions exhibited a 0-0 emission peak at  $\sim 2.30$  eV (FWHM = 0.083 eV) followed by the vibronic replica peaks with an energy spacing of  $\sim 0.14$  eV and Huang-Rhys factor of 0.64 (Fig. S5).

In all three diF R-ADT derivatives under study, the PL emission in solutions at concentrations below  $\sim 1$  mM was mono-exponential [ $\sim \exp(-k_{FC}t)$ , where  $k_{FC}$  is the decay rate] [Fig. 3(b)]. This is consistent with a single emissive species attributed to the FC states described above. The excited state lifetime ( $\tau_{FC} = 1/k_{FC}$ ) at low concentrations ( $\sim 10$   $\mu$ M) was  $\tau_{FC} = 10 \pm 1$  ns, consistent with previous studies of diF R-ADT molecules in solutions, which corresponds to the decay rate of  $k_{FC} = 0.10$  ns<sup>-1</sup>.<sup>36,56,57</sup> In the intermediate concentration range ( $\sim 1$  mM to  $\sim 10$  mM), this rate slightly decreased, yielding, for example, 0.069 ns<sup>-1</sup> at 5 mM for diF TES-ADT. This decreasing rate could be due to the contribution of re-absorption and re-emission events to the PL causing a slightly delayed emission. In the case of diF TBDMS-ADT, the PL dynamics at

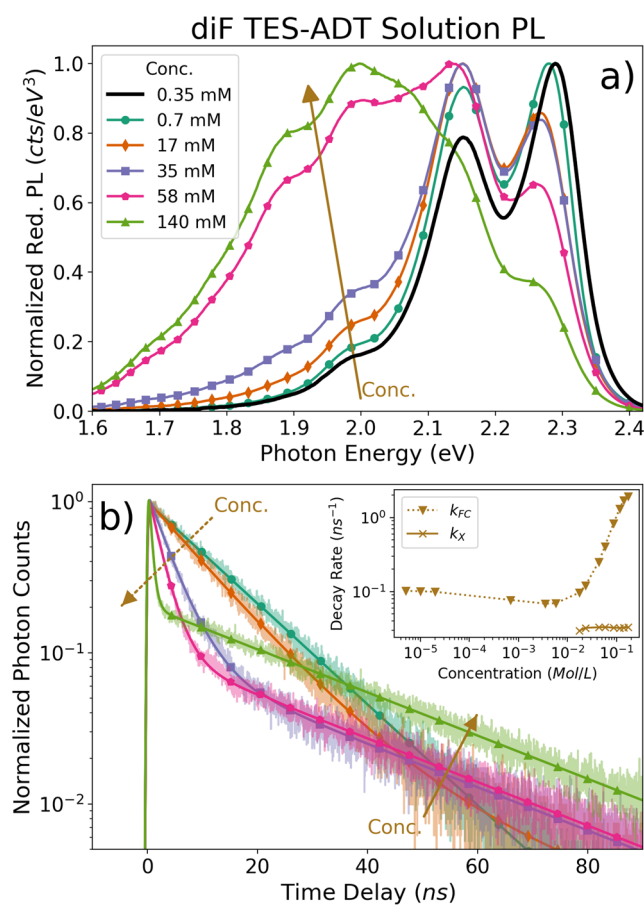


**FIG. 3.** The (a) normalized reduced steady-state photoluminescence (PL) and (b) time-resolved PL for solutions of diF TES-ADT in chlorobenzene at several concentrations. In (a), steady-state PL spectra show that as concentration increases, a new emission peak at  $\sim 2.0$  eV, attributed to an excimer (X), increases relative to the FC vibronic progression. In (b), time-resolved PL data are shown with low opacity, and fits of the data are overlaid as solid lines. The dotted (solid) arrow indicates the shortening of the FC lifetime (rising X weight) as concentration rises. The inset shows the extracted decay rates for the FC (dotted line with diamonds) and X (solid line with crosses) components across the entire range of concentrations for diF TES-ADT; see Fig. S7 for all derivatives.

intermediate concentrations exhibited a small ( $<3\%$  of the total emission) contribution from a negative amplitude component (e.g., Fig. S6), which vanished at higher concentrations. Such behavior was previously attributed to the presence of an additional, indirect channel of populating the emissive state,<sup>58</sup> although further study is needed to ascertain the origin of this channel in diF TBDMS-ADT solutions. As the concentration exceeded  $\sim 10$  mM, in all three diF R-ADT derivatives, the PL kinetics evolved from single to bi-exponential ( $\sim(1 - \beta)k_{FC} \exp(-k_{FC}t) + \beta k_X \exp(-k_X t)$ ), with the fast decay component ( $k_{FC}$ ) due to the FC emission and the new slow component with the rate  $k_X$  and weight  $\beta$  due to the formation of excimer (X) states [Fig. 3(b)]. In this high concentration regime ( $\sim 10$  mM and higher), the FC decay rate exhibited a strong

concentration dependence [inset of Figs. 3(b), S7, and S8], which was well described by the following relationship:

$$k_{FC}(C) = k^* \left( 1 + \left( \frac{C}{C_0} \right)^\gamma \right). \quad (1)$$

Here,  $C$  is the concentration of diF R-ADT molecules,  $C_0$  is a scaling factor,  $k^*$  is the decay rate at low concentrations, and  $\gamma$  is the power-law exponent. For example, for diF R-ADT with  $R = \text{TES}$  and  $\text{TSBS}$  in chlorobenzene, the fits of the data to Eq. (1) yielded an exponent  $\gamma = 1.77 \pm 0.01$  ( $1.70 \pm 0.01$ ) and a rate  $k^* = 0.0646 \pm 0.0001 \text{ ns}^{-1}$  ( $0.0650 \pm 0.0001 \text{ ns}^{-1}$ ) for  $R = \text{TES}$  ( $R = \text{TSBS}$ ), exhibiting only a weak dependence of these parameters on the side group  $R$  [inset of Fig. 3(b) and Fig. S8]. This suggests that the mechanism of excimer formation in solution is the same for these two side groups ( $R$ ) and is most likely a second-order diffusion-limited reaction similar to that seen in TIPS-Tc.<sup>59</sup> However, the side group does affect the concentrations at which excimer formation is activated, seen in the differing scale factors:  $C_0 = 24 \pm 4 \text{ mM}$  for  $R = \text{TES}$  and  $53 \pm 16 \text{ mM}$  for  $R = \text{TSBS}$ . diF TBDMS-ADT exhibits a slightly lower rate  $k^* = 0.0545 \pm 0.0001 \text{ ns}^{-1}$  and a scale factor  $C_0 = 30 \pm 5 \text{ mM}$  comparable with that in diF TES-ADT. However, the power-law exponent  $\gamma = 2.29 \pm 0.02$  is higher than that for diF TES-ADT and diF TSBS-ADT, which suggests that additional processes may be active with this molecule in highly concentrated solutions. See Fig. S8 for details on the fitting procedure.

The excimer (X) decay yielded a lower decay rate  $k_X$  of  $\sim 0.025 \text{ ns}^{-1}$ ,  $0.03 \text{ ns}^{-1}$ , and  $0.04 \text{ ns}^{-1}$ , corresponding to the lifetime of  $\sim 40 \text{ ns}$ ,  $30 \text{ ns}$ , and  $25 \text{ ns}$  for  $R = \text{TBDMS}$ ,  $\text{TES}$ , and  $\text{TSBS}$ , respectively—exhibiting only a weak concentration dependence up to  $\sim 0.1 \text{ M}$  concentration (Fig. S7). The weight  $\beta$  in the bi-exponential decay dynamics was strongly concentration-dependent, with the slower component due to the excimer emission dominating over the FC emission ( $\beta > 0.5$ ) at concentrations above the crossover concentration  $C_{\text{cross}}$  ( $41 \text{ mM}$ ,  $41 \text{ mM}$ , and  $59 \text{ mM}$  for  $R = \text{TBDMS}$ ,  $\text{TES}$ , and  $\text{TSBS}$ , respectively) and approaching 1 as the concentration approached  $0.1 \text{ M}$  (Fig. S9). This change in the excited state dynamics was accompanied by a change in the PL spectra [Fig. 3(a)], which developed a broad red-shifted component centered at about  $2 \text{ eV}$ , consistent with the excimer emission. The relative contribution of this excimer emission to the PL spectra increased with concentration relative to the FC vibronic progression and dominated the spectra at concentrations above the crossover concentrations  $C_{\text{cross}}$ , consistent with the trends seen in the PL dynamics. This can be seen in Fig. 3(a) for diF TES-ADT, where the broad emission peak at  $\sim 2 \text{ eV}$  rises drastically between the  $35 \text{ mM}$  and  $58 \text{ mM}$  concentrations. The larger values of  $C_0$  and  $C_{\text{cross}}$  for diF TSBS-ADT as compared to those in diF TES-ADT and diF TBDMS-ADT suggest that upon diffusive motion of the molecules in solution, it is statistically more probable to achieve a dimeric molecular configuration conducive to stable excimer formation in diF TES-ADT and diF TBDMS-ADT than in diF TSBS-ADT.

## B. Optical properties of crystals

### 1. Optical absorption

The optical absorption of diF R-ADT crystals differed from those of solutions and depended on the side group  $R$  [Fig. 1(a)].

We quantify these differences in three ways: (1) the solution-to-crystal shift ( $\Delta_{\text{StoC}}$ , defined as the energy difference between the lowest energy absorption resonances in solution and crystal), (2) the Davydov splitting ( $\Delta_{\text{DS}}$ ), and (3) the polarization dependence of the corresponding absorption spectral features. The relevant parameters are summarized in Tables I and SI and are discussed next.

*a. Optical absorption for diF TSBS-ADT crystals.* Among the three diF R-ADT derivatives, diF TSBS-ADT crystals exhibited an absorption spectrum most similar to that of dilute solutions [e.g., Fig. 1(a)]. In this derivative, the solution-to-crystal shift, due to non-resonant effects caused by the Coulomb interaction of the molecule with its surrounding and exchange interactions between translationally equivalent molecules, was only  $\Delta_{\text{StoC}} \sim 0.039$  eV. This is considerably smaller than that in diF TES-ADT and diF TBDMS-ADT crystals where the values of 0.105 eV and 0.16 eV, respectively, were obtained. The most important feature of the absorption spectra of all diF R-ADT crystals was in the presence of in-plane polarization dependence of the crystal spectra (Figs. 4–6 and S10–S12), which is discussed next.

In diF TSBS-ADT crystals, Davydov splitting ( $\Delta_{\text{DS}}$ ) of 0.045 eV was observed upon deconvolution of the lowest-energy absorption peak (Fig. S10), with the Davydov components, 1A and 1B [Fig. 4(a)], polarized at  $41^\circ$  (2.32 eV) and  $74^\circ$  (2.36 eV) with respect to the long crystal axis [Figs. 4(b) and 4(c)]. These two components were also highly anisotropic, with an anisotropy factor ( $A_{\text{max}} - A_{\text{min}})/(A_{\text{max}} + A_{\text{min}})$  of 0.93 and 0.71, respectively. The Davydov splitting results from interaction of translationally inequivalent molecules in crystals with  $Z > 1$ ; in acenes, it increases with the size of the molecule and with the degree of admixture between Frenkel

and CT states.<sup>12,18,59</sup> The  $\Delta_{\text{DS}}$  value obtained in diF TSBS-ADT is considerably lower than those observed in Tc, Pn, or Hex crystals with  $Z = 2$  (e.g., 0.08 eV, 0.14 eV, and 0.18 eV, respectively, in Refs. 21, 60, and 61) but comparable with that for the  $\alpha$ -phase perylene ( $Z = 4$ , same as that in diF TSBS-ADT) of 0.033 eV.<sup>26</sup>

The next higher energy state, peak 2 at  $\sim 2.5$  eV in Fig. 4(a), had a similar dominant polarization to that of peak 1B [Fig. 4(d)], but it exhibited a considerably lower anisotropy factor of 0.33. Peak 3 at  $\sim 2.7$  eV in Fig. 4(a) continued this trend, being nearly isotropic, with an anisotropy factor of only 0.18 [Fig. 4(e)]. Interestingly, peak 3 and all higher energy states [peaks 4 and 5 in Fig. 4(a)] exhibited distinctly different polarizations from those of peaks 1A, 1B, and 2, with dominant contributions at  $150^\circ$ ,  $160^\circ$ , and  $164^\circ$ , for peaks 3, 4, and 5, respectively [Figs. 4(e)–4(g)].

*b. Optical absorption for diF TES-ADT crystals.* The diF TES-ADT crystals did not exhibit any Davydov splitting, as expected based on their crystal structure with  $Z = 1$ . The in-plane polarization dependence of the optical absorption spectra revealed that the lowest energy (2.25 eV) absorption [peak 1 in Fig. 5(a)] was polarized at about  $80^\circ$  with respect to the long crystal axis, which is close to the short crystal axis [Figs. 5(b) and S12]. In agreement with our previous publication,<sup>54</sup> higher energy states contained contributions with different polarizations such that the dominant absorption at, for example, 2.41 eV and 2.57 eV [peaks 2 and 3 in Fig. 5(a)] was along  $90^\circ$  and  $100^\circ$ , respectively [Figs. 5(c) and 5(d)]. Additionally, the polarization of each peak from 1 to 4 followed a consistent trend, starting at  $84^\circ$  for peak 1 and steadily increased to  $110^\circ$  for peak 4. The anisotropy factors for peaks 2–4 were smaller than that of peak 1 (0.77–0.82 compared to 0.92) but did not have

**TABLE I.** Summary of basic optical and PL properties of diF R-ADT (R = TSBS, TES, and TBDMS) crystals. The solution-to-crystal shift was calculated as the difference between the lowest energy peak (1 or 1A) and the 0-0 line extracted from diF TES-ADT in dilute solution (Fig. S5). The Stokes shift was calculated between the lowest energy peak (1 or 1A) and the energy of the PL maximum at room temperature. The Davydov splitting was calculated as the difference between the transition energies of 1A and 1B (where applicable). The transition energies for each peak were calculated for diF TSBS-ADT and diF TES-ADT through a full deconvolution of the absorption spectra (see Figs. S10 and S11), whereas the values for diF TBDMS-ADT were extracted from a partial deconvolution, explained in the supplementary material. The PL lifetimes at low temperatures were extracted for the fast ( $k_1$ ), intermediate ( $k_2$ ), and slow ( $k_3$ ) components using maximum likelihood estimation on the band-edge emission, as described in the supplementary material.

Side group		R = TSBS	R = TES	R = TBDMS
Packing structure		“Sandwich-herringbone”	“Brickwork”	“Twisted-columnar”
Z		4	1	4
Solution-to-crystal shift		0.039 eV	0.105 eV	0.16 eV
Stokes shift		0.058 eV	0.13 eV	0.078 eV
Davydov splitting		0.045 eV	N.A.	0.09 eV
Absorption transition energy for peak 1	1A	2.32 eV	2.25 eV	2.19 eV
	1B	2.36 eV		2.28 eV
Emission maximum energy at T = 293 K		2.26 eV	2.12 eV	2.12 eV
PL lifetime at T = 78 K	$1/k_1$	2.45 ns	760 ps	610 ps
	$1/k_2$	8.71 ns	5.05 ns	2.79 ns
	$1/k_3$	29.8 ns	22.6 ns	16.4 ns

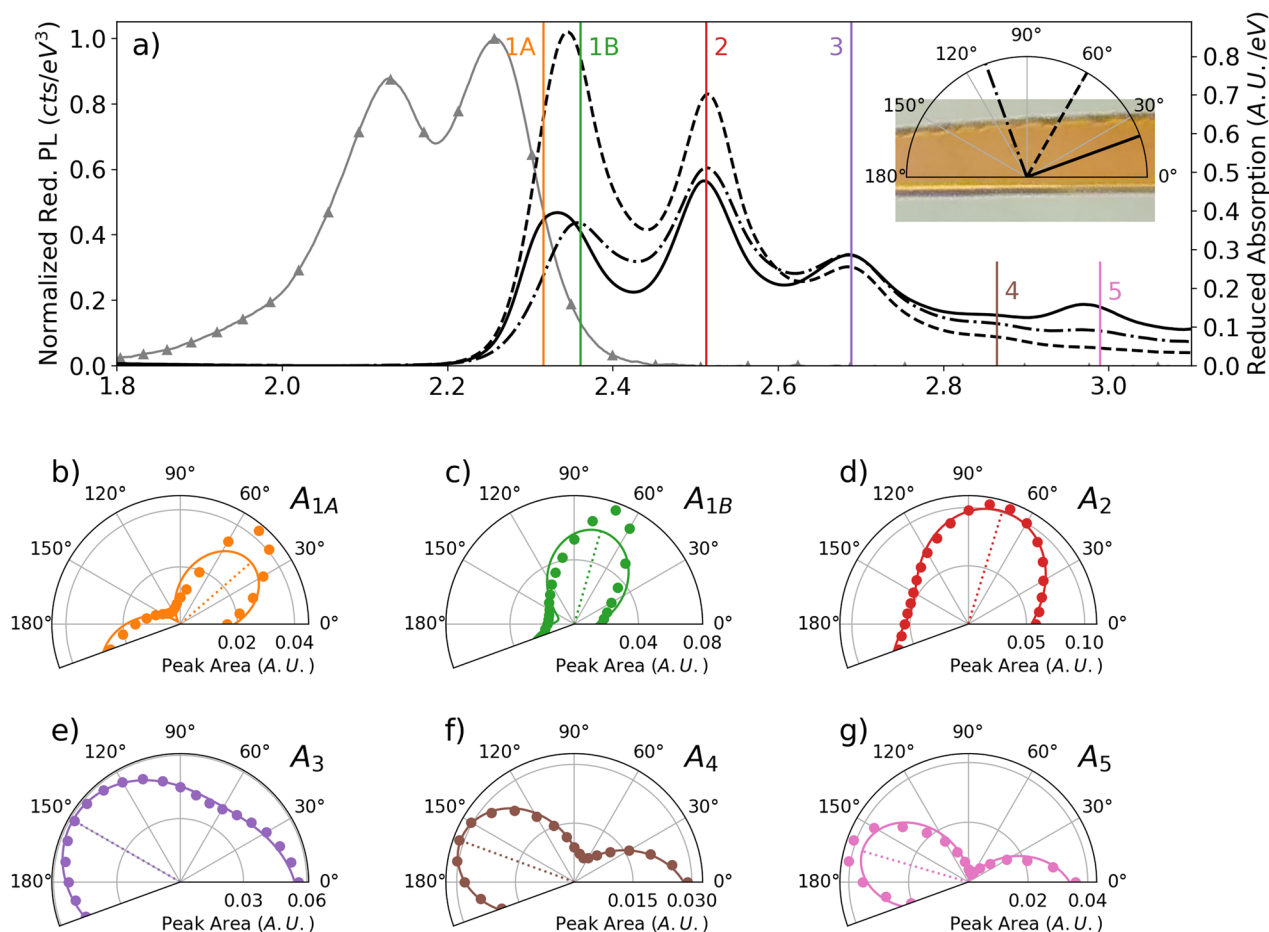


**FIG. 4.** (a) Normalized steady-state PL (triangles) and polarized absorption spectra at three representative polarizations (lines) for a single crystal of diF TSBS-ADT at room temperature. The inset shows a microscope image of the crystal, with an overlay showing the polarization orientation relative to the "long axis" of the crystal. The vertical bars label the energies of the absorptive states in the crystal, based on a full deconvolution of the absorption spectra (details in the [supplementary material](#)). The lowest-energy absorptive feature has two closely spaced resonances, 1A and 1B, comprising the Davydov pair in this system. [(b)–(g)] Polar plots showing the total area of the absorptive resonance peaks of (a) as a function of polarization. Extracted peak areas are given as dots, and fits according to Eq. (S5) are given as solid lines. The dotted radial line shows the polarization of maximum absorption.

the same clear ordering as in diF TSBS-ADT. Conversely, peak 5 did not exhibit either trend but returned to a very high anisotropy factor of 0.98, polarized at  $100^\circ$ . Interestingly, unlike the strong in-plane anisotropy, the out-of-plane anisotropy was relatively low (Fig. S14) as evidenced by pMAIRS where the overall absorption line shape remained unchanged across a range of angles of incidence.

*c. Optical absorption for diF TBDMS-ADT crystals.* The diF TBDMS-ADT crystals exhibited the most drastic deviation of the absorption spectra from those of solutions. In addition to the large solution-to-crystal shift  $\Delta_{\text{StoC}}$  of 0.16 eV, the peak sequence did not conform to the equally spaced replica peaks expected from a vibrationally coupled exciton. Instead, two broad features (centered at

about 2.27 eV and 2.7 eV) and a much narrower feature (at about 2.45 eV) were observed. In this case, full spectral deconvolution such as that of diF TSBS-ADT and diF TES-ADT (described in [supplementary material](#), Figs. S10 and S11) was not possible, and so, a partial deconvolution was utilized, as described in the [supplementary material](#) (Fig. S15). [Figures 6\(b\)–6\(g\)](#) show the polarization dependence of absorption at the particular wavelengths representative of each of the absorptive resonances labeled in [Fig. 6\(a\)](#). This revealed that both of the broad features ( $\sim 2.27$  eV and 2.7 eV) contained a finer structure, for example, Davydov pair 1A and 1B in the case of the lower-energy feature [[Fig. 6\(a\)](#)]. All resonances 1A–4 in the absorption spectra in [Fig. 6\(a\)](#) were predominantly polarized at  $90^\circ$  with respect to the long axis (*a*-axis) of the crystal but with changing anisotropy. In particular, the anisotropy factors started at 0.78 and 0.81 for Davydov pair 1A and 1B but steadily decreased

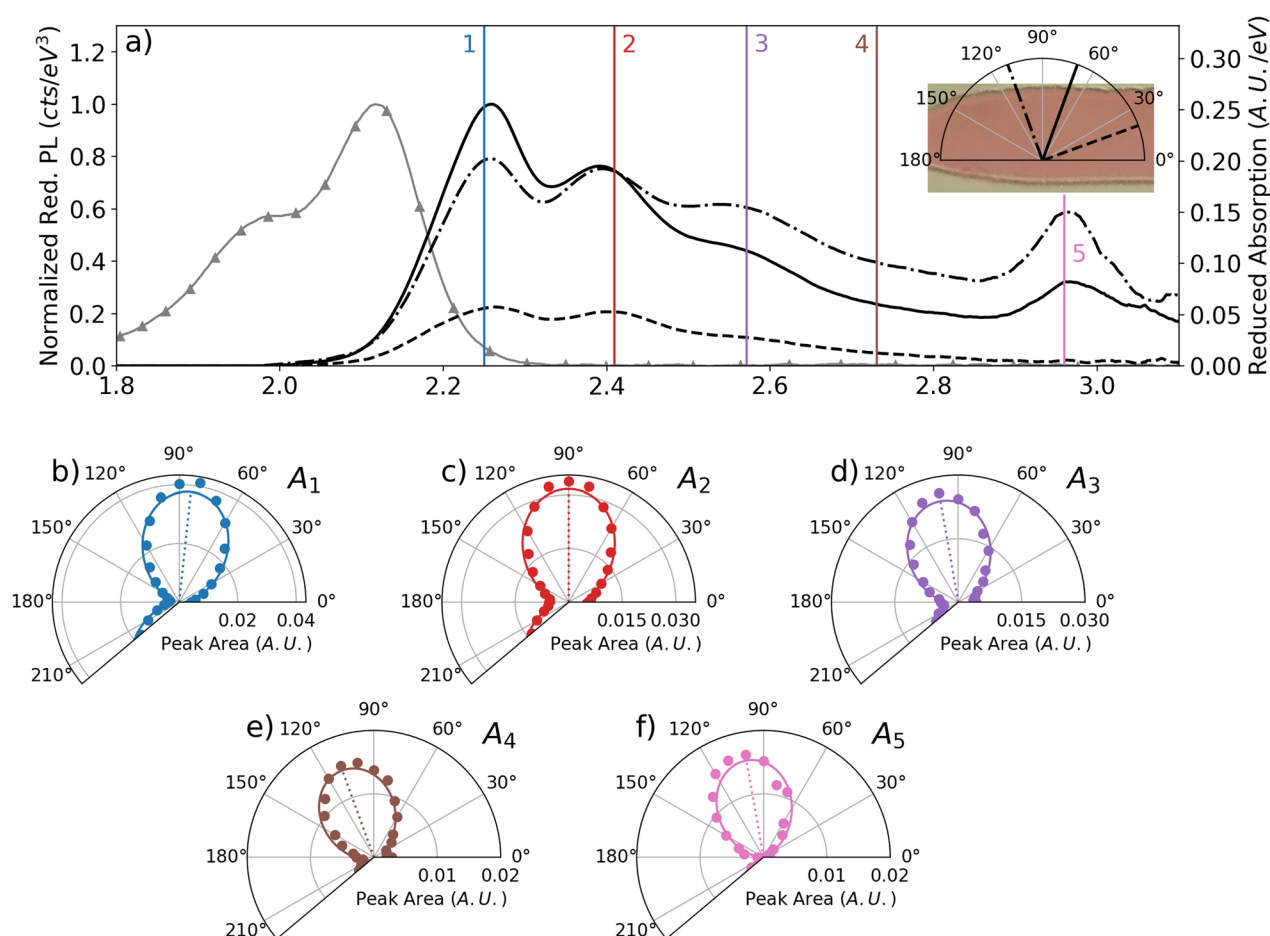


**FIG. 5.** (a) Normalized steady-state PL (triangles) and polarized absorption spectra, at three representative polarizations (lines), from a single crystal of diF TES-ADT at room temperature. The inset shows a microscope image of the crystal, with an overlay showing the polarization orientation relative to the “long axis” of the crystal. The vertical bars label the energies of the absorptive states in the crystal, based on a full deconvolution of the absorption spectra (details in the [supplementary material](#)). [(b)–(g)] Polar plots showing the total area of the absorptive resonance peaks of (a) as a function of polarization. Extracted peak areas are given as dots, and fits according to Eq. (S5) are given as solid lines. The dotted radial line shows the polarization of maximum absorption.

to only 0.40 for peak 3 similar to diF TSBS-ADT crystals. It should be noted that while peak 5 had a very low anisotropy factor (0.15), this is likely artificially low because the wavelength methods used for diF TBDMS-ADT do not deconvolve the spectra, so peak 5 contains some of the tail for peak 4. The Davydov splitting of 0.09 eV was obtained in diF TBDMS-ADT from partial deconvolution, which is considerably higher than that in diF TSBS-ADT (0.045 eV) and similar to that in Tc crystals (0.08 eV).

## 2. Photoluminescence

Similar to optical absorption, the steady-state PL from diF R-ADT crystals was strongly dependent on the side group R [Fig. 7(a)] and by extension the packing structure. Many trends observed in the absorption spectra were also seen in the PL. In particular, diF TSBS-ADT crystals had the most similar PL spectra to those in solution,

with only a small solution-to-crystal shift of <0.03 eV (which represents an upper bound due to self-absorption) and a similar line shape structure that included two main emission peaks at ~2.3 eV and ~2.1 eV with a shoulder at ~1.95 eV. On the other hand, both diF TES-ADT and diF TBDMS-ADT crystals had much larger PL spectral shifts (0.2 eV solution-to-crystal shift) and suppressed vibronic replica emission. For example, the diF TBDMS-ADT crystal had a dominant emission peak at 2.1 eV and only a weak shoulder near 1.9 eV [Fig. 7(a)].

The PL for each crystal was also strongly dependent on temperature, in several ways: an overall increase in the total emission and redshift of the spectra at lower temperatures (Fig. S16) were observed, and they were accompanied by changes in the line shape (i.e., relative contributions of various peaks to the overall PL spectra) (Figs. 8 and 9). In diF TES-ADT and diF TBDMS-ADT crystals, as the temperature decreased, the contribution of the low-energy

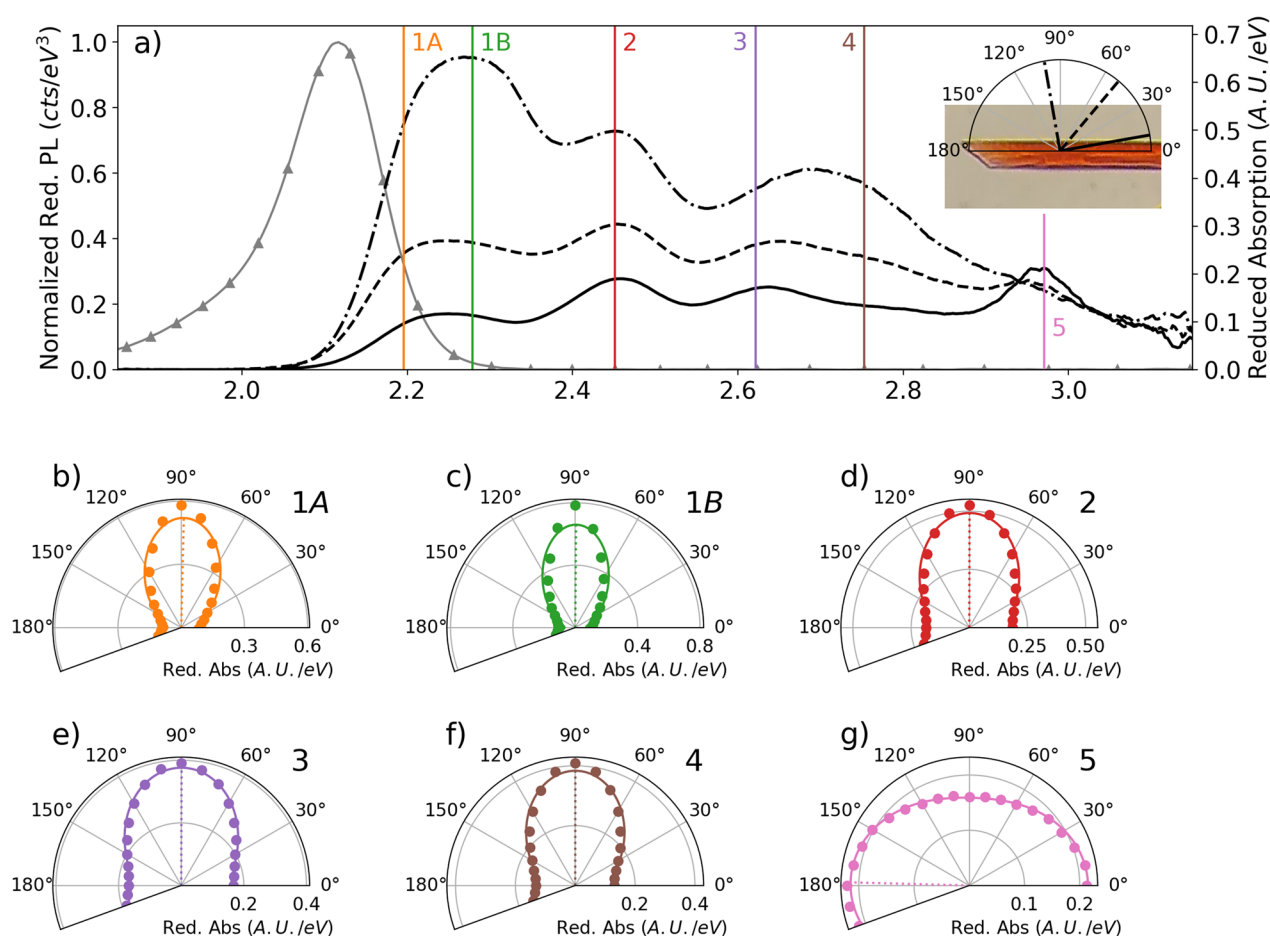


**FIG. 6.** (a) Normalized steady-state PL (triangles) and polarized absorption spectra, at three representative polarizations (lines), from a single crystal of diF TBDMS-ADT at room temperature. The inset shows a microscope image of the crystal, with an overlay showing the polarization orientation relative to the “long axis” of the crystal. The vertical bars label the median energies of the absorptive states in the crystal, based on a partial deconvolution of the absorption spectra (details in the [supplementary material](#)). The lowest energy absorptive feature has two closely spaced resonances, 1A and 1B, comprising the Davydov pair in this system. [(b)–(g)] Polar plots showing the reduced absorption at the median peak energy labeled in (a) as a function of polarization. The reduced absorption values are given as dots, and fits according to Eq. (S5) are given as solid lines. The dotted radial line shows the polarization of maximum absorption.

shoulders at 1.9 eV to the overall spectra increased, as seen from [Figs. 8\(a\)–8\(d\)](#).

In each derivative, the analysis of the PL dynamics [e.g., [Fig. 7\(b\)](#)] revealed that both a mono- and a bi-exponential model were insufficient to describe the full temperature- and wavelength-dependent PL dynamics. As discussed fully in the [supplementary material](#) ([Figs. S17 and S18 and Table SII](#)), we identified three emissive states (characterized by three distinct decay rates  $k_1$ ,  $k_2$ , and  $k_3$ ) with relative weights depending on the emission wavelength and temperature ([Figs. 8 and 10](#)).

[Figures 8\(a\) and 8\(b\)](#) show the reconstructed PL spectra (that is, the wavelength-dependent decay component weights rescaled by the steady-state PL spectra; details explained in [supplementary material](#), e.g., [Fig. S18](#)) of the three states obtained in a diF TES-ADT crystal at 293 K and 78 K. The “fast” decay component, with a lifetime

( $1/k_1$ ) of 0.49 ns (0.76 ns) at 293 K (78 K), adopted the same general structure as the steady-state PL (a main 0-0 emission peak at 2.1 eV and a shoulder due to the 0-1 vibronic replica peak at ~1.9 eV) and exhibited temperature dependence resembling that of delocalized excitons in J-aggregates, with the relative contribution of the 0-0 emission increasing at lower temperatures. In this case, the change in the relative 0-0 and 0-1 peak areas is related to the coherence size of the excited state, and the thermal coherence number ( $N_{\text{coh}}$ ) can be determined as follows:<sup>2</sup>

$$N_{\text{coh}} = \lambda^2 \frac{I_{00}}{I_{01}}, \quad (2)$$

where  $\lambda^2$  is the HR factor (assumed to be the same as for diF R-ADT molecules in dilute solution, 0.69) and  $I_{0i}$  is the area of the

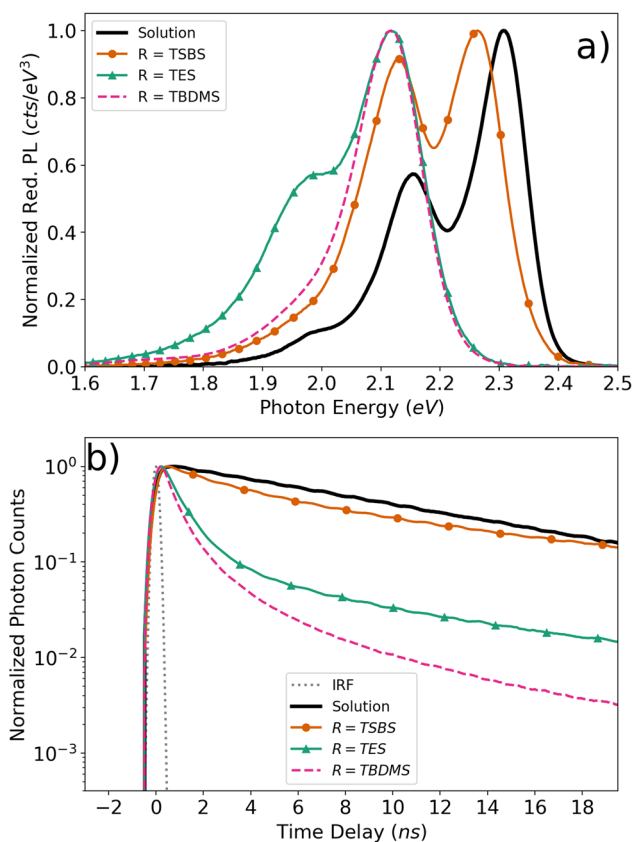


**FIG. 7.** Normalized steady-state (a) and time-resolved (b) photoluminescence of diF R-ADT in solution ( $R = \text{TSBS}$ , 0.18 mM in chlorobenzene; solid line) and in the crystal phase [ $R = \text{TSBS}$  (dots), TES (triangles), TBDMS (dashed line)] at room temperature. In (b), time-resolved PL is plotted as normalized photon counts, integrated over all wavelengths. The lines show the experimental data, smoothed for clarity (for fits, see the discussion in the [supplementary material](#)). The instrument response function (IRF) is included as a dotted line. The solution has the longest average PL lifetime, followed closely by diF TSBS-ADT, then diF TES-ADT, and finally, diF TBDMS-ADT crystals.

$i$ th peak. The  $N_{\text{coh}}$  calculated for diF TES-ADT from Eq. (2) yielded a weakly temperature-dependent value of  $\sim 1.6$ – $1.7$  (Fig. S19). The relative weight of this “fast” decay was dominant across the entire temperature range [Fig. 10(a)]. The “intermediate” decay component, with a lifetime ( $1/k_2$ ) of 1.8 ns (5.05 ns) at 293 K (78 K), exhibited a line shape change with temperature resembling that of the excitons in disordered H-aggregates.<sup>2</sup> In particular, at a low temperature (78 K), the PL of this component was principally at  $\sim 1.9$  eV (which corresponds to the 0–1 vibronic peak), but as the temperature increased, the contribution of the 0–0 emission peak at  $\sim 2.1$  eV grew and became dominant at 293 K, as shown in Fig. 9(b), with the activation energy for the thermally activated 0–0 transition of  $\sim 0.06$  eV (see the [supplementary material](#)). The “slow” component, with a lifetime ( $1/k_3$ ) of 13 ns (23 ns) at 293 K (78 K), showed a broad emission peak around 1.9 eV at a low temperature [78 K, see Fig. 8(a)] as well as a small emission at the 0–0 transition energy

( $\sim 2.1$  eV). As the temperature increased, the weight of this component in the overall PL dropped precipitously, accounting for less than 10% of the total emission near room temperature [Fig. 10(a)].

In diF TBDMS-ADT crystals, the three PL decay components followed similar trends overall [Figs. 8(c), 8(d), and S20] to those in diF TES-ADT but with a few notable differences. The first difference was that the lifetimes of each of the three components were shorter than those of diF TES-ADT (at 293 K,  $1/k_1 = 0.33$  ns,  $1/k_2 = 1.5$  ns, and  $1/k_3 = 7.5$  ns). Additionally, the “intermediate” and “slow” components constituted a considerably smaller percentage of the total emission compared with diF TES-ADT, making up only 25% and 8%, respectively, of the total PL at low temperatures, which further decreased as the temperature increased (down to 5% and 3%, respectively, at 293 K). The line shape of the “fast” component had a temperature dependence qualitatively similar to that of diF TES-ADT, with the  $I_{00}/I_{01}$  emission peak ratio increasing as the temperature decreased [Fig. 9(a)], but with a considerably more pronounced change as compared to that in diF TES-ADT. In particular, in diF TBDMS-ADT, the thermal coherence number [ $N_{\text{coh}}$  of Eq. (2)] varied with the inverse square root of temperature ( $T$ ), which is consistent with the model for 1D J-aggregates,<sup>2</sup>

$$N_{\text{coh}} = N_{\infty} + \sqrt{\frac{4\pi E_c}{k_B T}}, \quad (3)$$

where  $N_{\infty}$  is the coherence number in the thermodynamic limit found to be  $1.1 \pm 0.4$  (consistent with the theoretical value of 1),  $E_c$  is the curvature of the exciton band found to be  $17.5 \pm 0.5$  meV, and  $k_B$  is the Boltzmann constant. The inset of Fig. 9(a) illustrates the fit of the data with Eq. (3), showing a good agreement with this model and predicting a coherence size of  $\sim 7$  molecules at 78 K, which reduces to  $\sim 4$  molecules at 293 K. Similar to diF TES-ADT, the “intermediate” component exhibited temperature-dependent PL spectra resembling that of H-aggregates, with the 0–0 transition thermally activated with an activation energy of  $\sim 0.02$  eV (Fig. S21).

The key features in the dynamics of the diF TSBS-ADT emission were the absence of a fast, sub-nanosecond decay component (so that the three components had lifetimes of  $1/k_1 = 2.5$  ns,  $1/k_2 = 8.7$  ns, and  $1/k_3 = 30$  ns at 78 K) and the large contribution of the “slow” component to the total PL even at higher temperatures [e.g.,  $\sim 30\%$  of the overall PL at 200 K, see Fig. 10(c)]. Additionally, the two faster components were similar in their line shape [with a preferential emission near the 0–0 PL emission, peaked at about 2.2 eV, Fig. 8(e)].

The temperature dependence of each of the three decay rates was well described as the sum of a temperature independent (static) rate  $k_S$  and thermally activated (dynamic) contribution with the rate  $k_D$  and activation energy  $E_a$ ,

$$k_{PL}(T) = k_S + k_D \exp\left(-\frac{E_a}{k_B T}\right), \quad (4)$$

where  $k_B$  is the Boltzmann constant. Figure S17 of the [supplementary material](#) shows the modeling procedure, and Table SII gives the values of  $k_S$ ,  $k_D$ , and  $E_a$  for each of the three decay components in each diF R-ADT derivative. The temperature dependence of the decay rates revealed the following distinct features of the

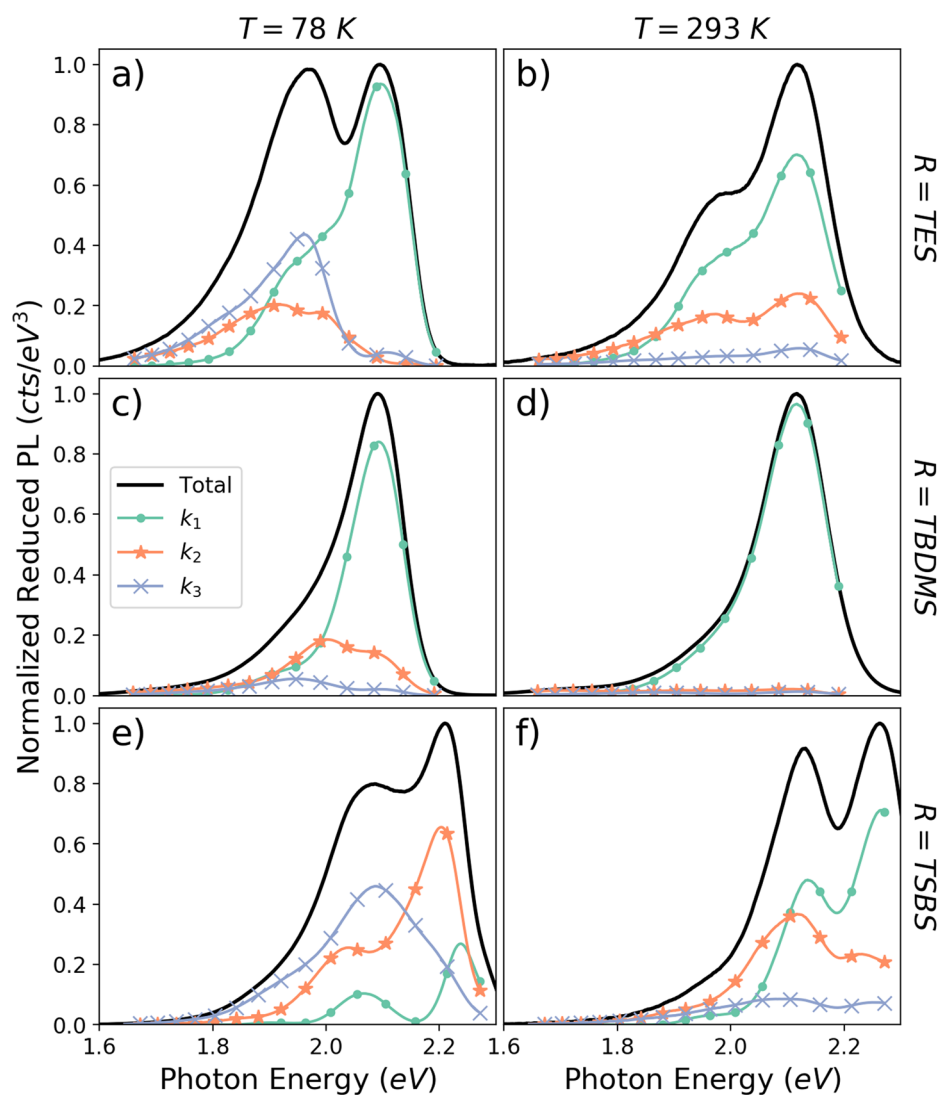


**FIG. 8.** The reconstructed photoluminescence spectra for the three decay components ( $k_1$ ,  $k_2$ ,  $k_3$ ) for diF R-ADT ( $R = \text{TES}$ ,  $\text{TBDMS}$ , and  $\text{TSBS}$ ) at low (78 K) and high (293 K) temperatures. Plotted also is the steady-state PL (the “total” PL) at that temperature. Data are normalized so that the steady-state PL (which is used to scale the wavelength-dependent decay component weights—called the “reconstructed PL”; see the [supplementary material](#)) is set to a maximum value of 1.

PL dynamics in diF R-ADT crystals: (1) the “fast,” sub-nanosecond decay component in diF TES-ADT and diF TBDMS-ADT was only weakly temperature dependent ( $E_a = 0.004$  eV and  $0.016$  eV, respectively), (2) the activation energy of the “intermediate” and “slow” decay components in diF TES-ADT was  $0.12$  eV and  $0.1$  eV, respectively, which are considerably higher than those in diF TBDMS-ADT ( $0.007$  eV and  $0.036$  eV, respectively), and (3) activation energies of the two faster decay rates in diF TSBS-ADT had similar values of  $0.029$  eV and  $0.032$  eV.

## IV. DISCUSSION

### A. Optical absorption

First, we briefly describe optical transitions in isolated diF R-ADT molecules. As detailed in Sec. III A, the absorption spectrum

of diF R-ADT in dilute solution in the  $2.3$  eV– $2.8$  eV range is well described by the zero-phonon (0-0) peak at  $2.355$  eV and its 0- $n$  ( $n = 1, 2, 3$ ) vibronic replica.<sup>54</sup> The next apparent transition in solution is that at  $2.98$  eV, with a considerably lower oscillator strength as compared to that of the 0-0 line [7% of the 0-0 peak area, Figs. 1(a) and S5]. The transitions at  $2.355$  eV and  $2.98$  eV are consistent with the two lowest allowed electronic transitions predicted by DFT (Table SIII), which will be referred to as  $S_0$ – $S_1$  and  $S_0$ – $S_2$  transitions, respectively. The transition dipole moment (TDM) for the  $S_0$ – $S_1$  transition is along the short molecular axis for the *syn*-ADT isomer and about  $15^\circ$  off the short axis for the *anti*-ADT (Fig. S2). For the  $S_0$ – $S_2$  transition, the TDMs are coincident with the long axis of the molecule for the *syn*-ADT; however, due to the inversion symmetry of the *anti*-ADT molecules, the second excited state is forbidden (Fig. S2). DFT also predicts that the *syn*-ADT  $S_0$ – $S_2$  oscillator strength should be 19% of the value of the  $S_0$ – $S_1$  oscillator

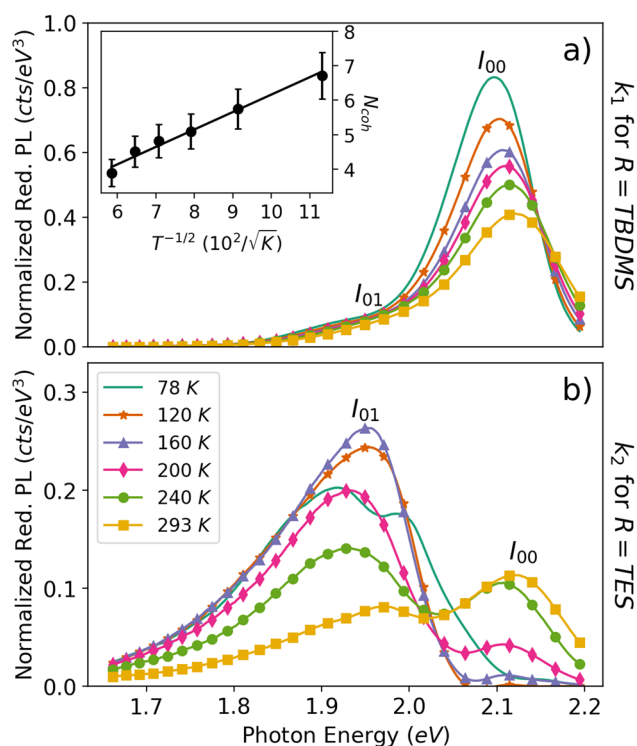


**FIG. 9.** (a) The temperature dependence for the reconstructed PL spectra of the delocalized Frenkel state ( $k_1$ ) in diF TBDMS-ADT. The spectra are normalized so that the steady-state PL (used to generate the reconstructed PL; see the [supplementary material](#)) at  $T = 78$  K is set to a maximum value of 1, so as to allow quantitative comparisons between temperatures. Labeled are the first two vibronic peaks:  $I_{00}$  and  $I_{01}$ . The inset shows a thermal coherence number of the Frenkel state (dots), calculated according to Eq. (2) from the experimental data, with error bars estimated at 10%. A fit according to Eq. (3) (line) is also included. (b) The temperature dependence for the reconstructed PL spectra of the  $^1(TT)$  state ( $k_2$ ) in diF TES-ADT. The spectra are normalized using the same scheme as (a). Labeled are the first two vibronic peaks:  $I_{00}$  (thermally activated) and  $I_{01}$ .

strength, which with the 65:35 mixture of *anti*- and *syn*-ADT predicts an absorbance ratio of 6.5% for the first and second excited states (in excellent agreement with our measured value of 7% for dilute solution, see Fig. S5).

### 1. Optical absorption for diF TES-ADT crystals

Next, we discuss the features of absorption spectra in diF TES-ADT crystals, which is the simplest case ( $Z = 1$ ) of the three derivatives under study. The analysis of the absorption spectra (Fig. 5) shows a clear absorption resonance at 2.96 eV [feature 5 in Fig. 5(a)], which we assign to the *second* electronic manifold—corresponding to the  $S_0$ – $S_2$  transition in solution (2.98 eV)—due to its close energy alignment with the  $S_0$ – $S_2$  transition. Additionally, the polarized absorption spectra indicate that the 2.96 eV state's TDM is consistent with the TDM of the *syn*-ADT  $S_0$ – $S_2$  transition [along the molecular backbone, Fig. S2(a)]. Figure 5(f) shows that the 2.96 eV state's TDM—when projected onto the optical ( $a$ – $b$ ) plane—is oriented at about  $100^\circ$  with respect to the long crystal axis (Table SI), which is the  $b$ -axis.<sup>45</sup> As can be appreciated from Fig. 2(a), this is

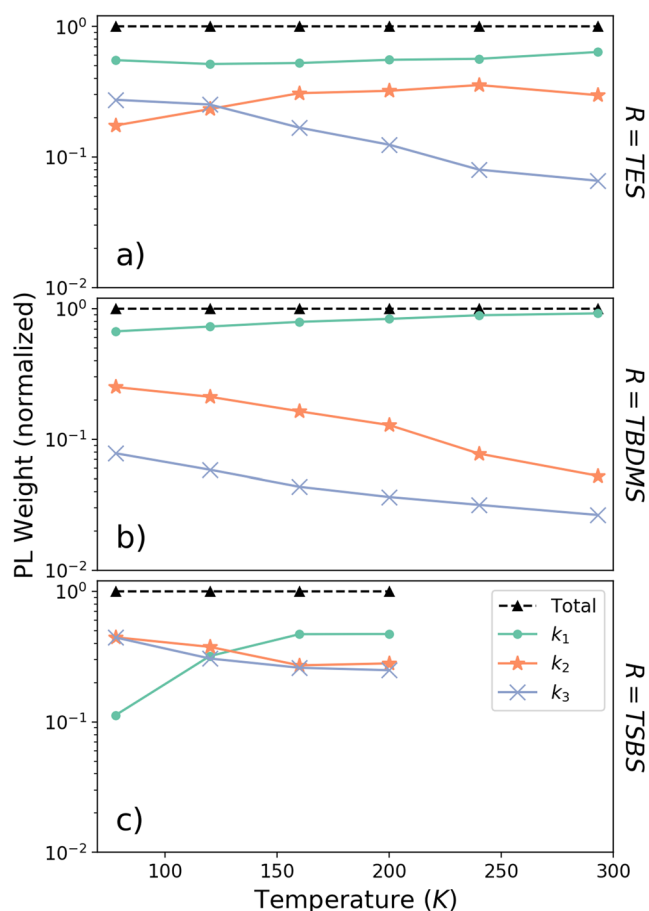


**FIG. 10.** The comparative weights of each of the three decay components ( $k_1$ ,  $k_2$ ,  $k_3$ ) based on the integrated reconstructed PL spectra for diF R-ADT ( $R = TES$ , TBDMS, and TSBS). Plotted are the reconstructed PL spectra integrated over wavelength and then normalized to the value of the integrated steady-state PL spectra (used to generate the reconstructed PL; see the [supplementary material](#)) at that temperature. This allows for the comparison of each component's proportional contribution to the total emission. For diF TSBS-ADT, this process was not possible above  $T = 200$  K due to a blue-shifting of the emission beyond the cut-off filter of the measurement system, which prevented accurate numerical integration of the highest energy emission peak.

nearly coincident with the orientation of the long dimension of the diF TES-ADT molecular backbones (which point at  $\sim 100^\circ$  measured clockwise off the  $b$ -axis).

The analysis of the absorption spectra (Fig. 5) together with pMAIRS (Fig. S14) results suggests the presence of two distinct electronic states within the 2.2 eV–2.8 eV range (corresponding to the  $S_0$ – $S_1$  electronic/vibrational energy manifold for isolated diF R-ADT molecules). These two states (2.25 eV and  $\sim 2.6$  eV, respectively) have distinct TDMs both in terms of their in-plane and out-of-plane orientations evidenced by the differing polarization dependence of the first four absorption peaks [peaks 1–4 in Figs. 5(a) and S12]. Dimer TD-DFT calculations also predict two kinds of excited states in this same energy range (2.0 eV–2.8 eV). The first kind are Frenkel-type

excitons [where the electron and hole wavefunctions, extracted from the Natural Transition Orbitals (NTOs), are primarily located on the same molecule in the dimer; see the [supplementary material](#)], with TDMs approximately parallel to the short dimension of the diF TES-ADT molecular backbone [cf.  $S_0$ – $S_1$  in Fig. S2(a) and  $F^{(1)}$  in Fig. S22(a); note that perfect alignment of TDMs is not expected, as even the “Frenkel-type” excitons in dimers have a small CT character due to mixing, causing a perturbation of the TDM orientation]. Projection of these TDMs into the optical ( $a$ – $b$ ) plane of the crystal yields orientation of  $83^\circ$  off the  $b$ -axis (long axis) of the crystal, in excellent agreement with the experimental data ( $84^\circ$ ) for the lowest-energy (2.25 eV) absorption peak [peak 1 in Fig. 5(a)]. The second kind of excited state is charge transfer (CT) in character (with electron and hole wavefunctions located on different molecules in the dimer, e.g., Fig. S23). These CT states have considerably smaller TDMs than those of Frenkel states, and the CT TDMs are oriented in the intermolecular direction, rather than in the plane of either molecular backbone (Fig. S22). The largest of such CT TDMs has a projection on the optical ( $a$ – $b$ ) plane at about  $120^\circ$  with respect to the  $b$ -axis of the crystal [inset of Fig. 5(a)]. The TDM for the experimentally observed higher energy transition [e.g., peak 3 in Fig. 5(a)] in the optical plane ( $100^\circ$  off the  $b$ -axis) is between the calculated TDMs for the Frenkel and CT excitons, and so, we attribute this transition to the admixture of the Frenkel and CT states.

To further study the nature of these two states in diF TES-ADT, it is helpful to compare our observations to a similar crystalline system widely studied in the literature: a functionalized Pn derivative, TIPS-Pn.<sup>50,62</sup> Similar to diF TES-ADT, the TIPS-Pn exhibits a 2D “brickwork” molecular packing with the  $a$ – $b$  plane as a substrate plane of the solution-grown crystal. In Ref. 50, four distinct electronic states ( $S_1$ – $S_4$ ) were revealed in the 1.6 eV–2.5 eV range using the GW/BSE approach, with states  $S_1$  and  $S_4$  exhibiting similarly out-of-phase polarization dependence seen in our lower (2.25 eV) and higher (2.57 eV) energy states in diF TES-ADT. The theory predicted that while the lowest-energy ( $S_1$ ) state has a molecular origin and is due to coupling of light to the TDM along the short axis of the molecule, the higher-energy absorption features rely on the long-range order and  $\pi$ – $\pi$  overlap that causes the formation of many nearly degenerate excited state transitions. The electron–hole correlation function for these predicts higher exciton delocalization than that of the  $S_1$  state. In other studies, such as those of optical properties of Pn, TIPS-Pn, and rubrene, two distinct electronic states separated by about 0.3 eV–0.35 eV, and of different nature, were observed.<sup>17,18,62,63</sup> For example, in Pn crystals, the lower-energy exciton was primarily of Frenkel character and the 0.35 eV–offset higher-energy exciton was primarily of CT character,<sup>18</sup> which is comparable to our observations in diF TES-ADT.

## 2. Optical absorption for diF TSBS-ADT crystals

In the diF TSBS-ADT crystals ( $Z = 4$ , “sandwich-herringbone” packing), Davydov splitting of 0.045 eV was observed, with the projection of the TDM onto the optical (011) plane for the lower (higher) energy Davydov component aligned along  $41^\circ$  ( $74^\circ$ ) with respect to the long crystal axis [Figs. 4(b) and 4(c)]. The Davydov splitting arises from the interactions between pairs of inequivalent molecules inside the crystal unit cell. For example, in the  $Z = 2$

system of Pn,<sup>18</sup> two Davydov states were observed with TDMs corresponding to the symmetric ( $\mu_+$ ) and antisymmetric ( $\mu_-$ ) combinations of the individual molecular TDMs:  $\mu_\pm = \mu_1 \pm \mu_2$ . For diF TSBS-ADT where  $Z = 4$ , there are potentially six different inequivalent molecular pairs [two intra-chain, e.g., 1–2 and 2–3 in Fig. 2(c), and four inter-chain, e.g., 2–4 and 2–5 in Fig. 2(c)]. However, since all intra-chain molecules have the same orientation due to their glide reflection symmetry, the two molecular TDMs ( $\mu_1$  and  $\mu_2$ ) for any pair are parallel. This makes the anti-symmetric state dark (as seen in Table SIV with vanishing oscillator strength for the second Frenkel-type exciton in all intra-chain dimers). Since we do observe a Davydov pair, it must be due to the inter-chain dimers, which have distinct molecular TDMs admitting bright anti-symmetric states. TD-DFT calculations for inter-chain dimers confirm this by predicting two Frenkel-type states with nonzero oscillator strength (transitions at 2.229 eV and 2.239 eV, Table SIV) and TDMs whose projections onto the (011) plane of the crystal are aligned with the  $70^\circ$  and  $81^\circ$  with respect to the  $a$ -axis for the lower and higher Davydov states, respectively, for *syn*–*syn* ADT isomer dimers (Fig. S22). By assigning the  $a$ -axis to the fast growth direction of the crystal (long crystal axis), this provides qualitative agreement with the polarizations of the Davydov components seen in the absorption spectra [Figs. 4(b) and 4(c)], insofar as the pair of TDMs are both oriented off-axis and relatively close together ( $\sim 10^\circ$  separation predicted by calculation and  $\sim 30^\circ$  separation observed in the experiment). Differences between the theoretical and experimental orientations of the Davydov component TDMs could be partly due to the simplifying assumptions made in the TD DFT model, including the use of *syn*–*syn* ADT dimers in the calculation, whereas the diF TSBS-ADT crystal is a mixture of *syn*- and *anti*-ADT isomers. Since the *anti*-ADT isomer has a slightly different molecular TDM (see Fig. S2) compared to the *syn*-ADT isomer, the resulting symmetric and antisymmetric dimer TDMs that involve *anti*-ADT isomers are similarly shifted with respect to *syn*–*syn* dimers. Additionally, dimer-based calculations do not capture the full extent of the intermolecular interactions. Nevertheless, the simplified dimer-based approach here has been utilized by other studies<sup>62</sup> that have seen good agreement between TDMs predicted by TD-DFT and those extracted from experimentally measured polarized absorption. Simulating either a fully periodic system or a large cluster would be necessary to provide a more quantitative assessment of the impact of intermolecular interactions on the spectral features; however, both of these are computationally intensive and are beyond the scope of the present study.

In addition to the Davydov components (Frenkel-type excitons), diF TSBS-ADT crystals show evidence of Frenkel-CT mixing at higher energies. These CT states, such as in diF TES-ADT, appear to be higher in energy, near the 2.69 eV resonance [3 in Fig. 4(a)], and are due to intra-chain dimers. TD-DFT calculations on intra-chain dimers predict a CT-type exciton with a nonzero TDM aligned at  $\sim 160^\circ$  with respect to the  $a$ -axis [Fig. S22(b)]. This agrees well with the observed orientation of the experimentally observed TDM at  $150^\circ$  with respect to the long crystal axis ( $a$ -axis) for feature 3 [Fig. 4(e)], suggesting a large CT character to this state mediated by nonvanishing intra-chain electron and hole transfer integrals (see Sec. IV C for further discussion). Finally, the 2.98 eV absorption [peak 5 in Fig. 4(a)] in diF TSBS-ADT is polarized at  $165^\circ$  [Fig. 4(f)]. Similar to diF TES-ADT, this is consistent with the  $S_0$ – $S_2$  TDM

parallel to the long axis of the ADT molecular backbone, which makes a  $160^\circ$  angle with the  $a$ -axis of the diF TSBS-ADT crystal.

### 3. Optical absorption for diF TBDMS-ADT crystals

In the diF TBDMS-ADT crystals (“twisted columnar” packing motif), three main features were observed within the  $S_0$ – $S_1$  energy manifold [Fig. 6(a)]: two broad features (centered at about 2.27 eV and 2.7 eV) and a much narrower peak (at about 2.46 eV), all polarized predominantly at  $90^\circ$  with respect to the long axis ( $a$ -axis) of the crystal. This agrees reasonably well with TD-DFT predictions: given that the long ( $a$ -) axis of the crystal and the  $\pi$ – $\pi$  stacking direction of the columnar stacks are coincident [Figs. 2(e) and 2(f)], all projections of the Frenkel TDMs [Fig. S22(c)] onto the optical plane are oriented approximately perpendicular to the long axis of the crystal (since all the molecular backbones are normal to the  $a$ -axis). In particular, the broad 2.27 eV feature is asymmetric with a shoulder on the red edge [in that the peak is non-Gaussian, cf. 1A in Fig. 6(a)], with polarization-independent asymmetry (thus, similar polarization dependence of 1A and 1B in Fig. 6) but polarization-dependent total absorption [Fig. S12(c)]. This suggests the presence of two states of similar energy and with similar TDM orientations. We assign these states to a Davydov pair, arising from the inequivalent intra-column molecules [e.g., pair 1–3 in Figs. 2(e) and 2(f)]. Unlike diF TSBS-ADT, where intra-chain molecules all have the same orientation (causing the anti-symmetric dimer TDM to vanish), intra-column diF TBDMS-ADT molecules have a  $45^\circ$  twist between neighboring molecules. This ensures that for inequivalent dimers, both the symmetric and anti-symmetric states are bright. TD-DFT calculations confirm this, predicting nonzero oscillator strengths for both of the Frenkel-type excitons in intra-column inequivalent molecular pairs (Table SIV). The TDMs for these two Frenkel-type states also align well with the symmetric and anti-symmetric combinations of the molecular TDMs; however, when projected into the optical plane, these TDMs become nearly parallel and, thus, difficult to distinguish in polarization-dependent optical measurements. The Davydov splitting obtained from the deconvolution of the broad 2.27 eV peak yields  $\sim 0.09$  eV, which is twice as large as that in diF TSBS-ADT but is comparable to that in Tc crystals (0.08 eV)<sup>60</sup> and Pn crystals ( $\sim 0.11$  eV– $0.14$  eV).<sup>18,21</sup> The amount of Davydov splitting has been previously related to the degree of the CT and Frenkel exciton admixture.<sup>12,18,59</sup> Moreover, the recent work by Hestand and Spano<sup>2</sup> established that in the context of charge-transfer J-aggregates, strong Frenkel-CT mixing can produce a two-band absorption signature, where a pair of well-separated and dominant absorptive peaks is observed. These two peaks represent the two bright exciton bands that form as a result of the Frenkel and CT states mixing. The dominant presence of both low energy (2.27 eV) and high energy ( $\sim 2.7$  eV) absorptive features in the diF TBDMS-ADT spectra is indicative of exactly this behavior and suggests a strong mixing between the Frenkel and CT states in diF TBDMS-ADT. The CT character of exciton states in diF TBDMS-ADT can also be inferred from the variations of polarization anisotropy of peaks 1–4 in Fig. 6. With the columnar molecular packing of diF TBDMS-ADT [Fig. 2(c)], any intra-column CT state should have a TDM oriented in the  $\pi$ – $\pi$  stacking direction, making it approximately parallel to the  $a$ -axis of the crystal

(Fig. S22). Any Frenkel-CT mixing, then, would manifest as additional absorption along the long axis of the crystal, which is indeed observed for states 2–4, which exhibit reduced anisotropy factors [Table SI and Figs. 6(d)–6(f)].

Finally, it is interesting to note that the state corresponding to  $S_0$ – $S_2$  in solution (2.98 eV) was present in all diF R-ADT crystals under study and that its energy is relatively insensitive to the molecular side group (R). Additionally, its polarization in any of the crystals under study was always along the long axis of the molecule, which is the orientation of the  $S_0$ – $S_2$  TDM for isolated molecules. These observations indicate a negligible effect of intermolecular interactions on this state in diF R-ADT crystals, pointing to an intramolecular nature of this exciton, which is similar to observations in TIPS-Pn and TES-Pn crystalline films.<sup>62</sup>

### B. Emissive states in crystals

As discussed above, the PL emission from diF R-ADT crystals includes contribution of three electronic states, properties of which are molecular packing-dependent. Based on our observations of Figs. 7 and 8, we assign each of these states to one of the following (Fig. 11): (1) singlet (Frenkel) excitons, (2) entangled pairs of triplet excitons  $^1$ (TT),<sup>28</sup> and (3) self-trapped excitons (STEs) similar in character to the excimers observed in solution.<sup>23</sup> Before discussing properties of each of these states in our crystals, we comment on the general properties of  $^1$ (TT) and STE.

The triplet pairs  $^1$ (TT) are an intermediate state in the singlet fission (SF) process, and mechanisms of its formation and decay have been extensively discussed in the literature.<sup>8</sup> Recently, charge transfer directly from this state on donor molecules to an acceptor molecule has been demonstrated, which opens up possibilities to use molecules with a stable  $^1$ (TT) state as donors in donor-acceptor photovoltaic cells with SF-enabled enhanced photogeneration efficiencies.<sup>28</sup> It was also found that in diF TES-ADT and rubrene films, these correlated triplet pairs radiatively decay by two pathways. First, the  $^1$ (TT) state can borrow oscillator strength from nearby bright states through a Herzberg–Teller-like effect. This produces a vibronic progression, where the 0– $n$  ( $n = 1, 2, \dots$ ) transitions are allowed, but the 0–0 transition is suppressed. Second, with sufficient thermal energy, the  $^1$ (TT) state can “back-convert” to the emissive  $S_1$  state and emit via delayed fluorescence—notably via the 0–0 transition.<sup>28</sup> The combination of these two pathways manifests as a suppressed 0–0 emission at low temperatures that is thermally activated at sufficiently high temperatures. These features were observed in our diF TES-ADT [Figs. 8(a), 8(b), and 9(b)] and diF TBDMS-ADT [Figs. 8(c), 8(d), and S21] crystals, in the case of the “intermediate” PL decay component of the emission, as discussed below.

The emissive “excimer-like” STE states<sup>23</sup> in the crystal phase have been observed in various acene derivatives (including polycrystalline films of tetracene<sup>23</sup> and anthracene<sup>64</sup>); their formation was facilitated by polycrystalline interfaces, where adjacent molecules can have the face-to-face orientation (rather than the bulk face-to-edge orientation), which is necessary for large CT integrals. These CT integrals mediate the formation of excimer-like states, which have high CT character. The emission from these states is expected to be redshifted relative to the singlet states, to be structureless in

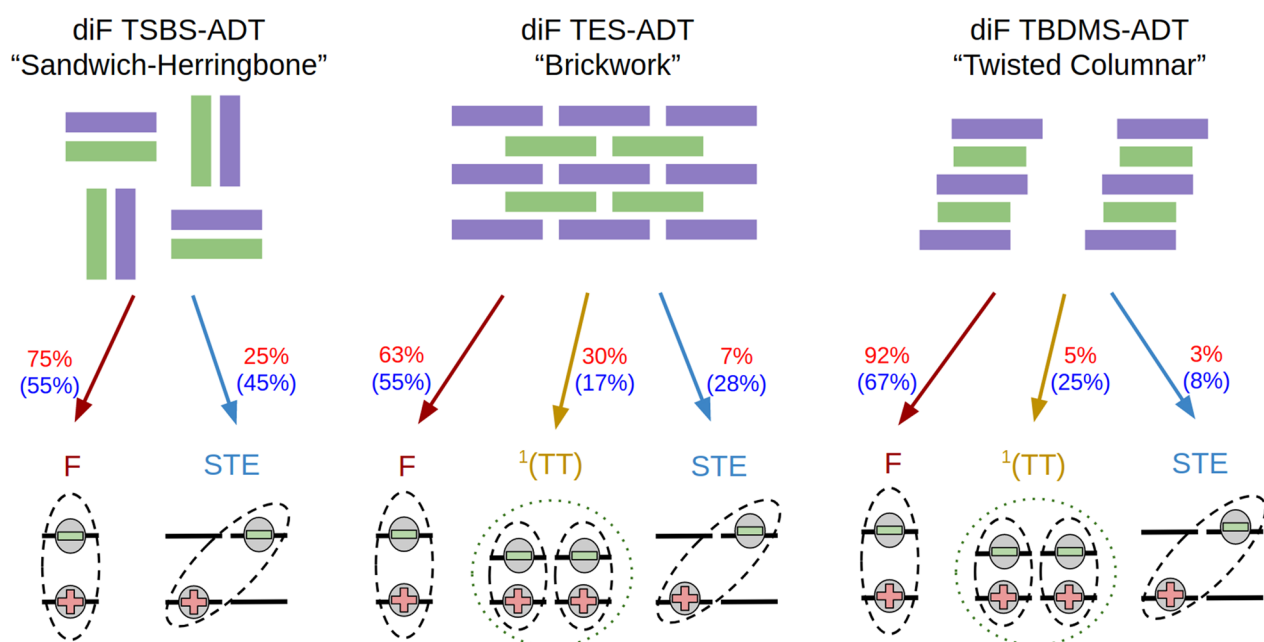


**FIG. 11.** Schematic representation of the relaxation pathways for diF R-ADT (R = TSBS, TES, and TBDMS). Each arrow shows the three radiative decay pathways: Frenkel (singlet), entangled triplet, and self-trapped exciton. Each arrow is labeled with the percentage of the total PL constituted by that pathway at  $T = 293$  K ( $T = 78$  K). Note that for diF TSBS-ADT,  $T = 200$  K is used instead of 293 K.

its line shape, and to possess a much longer state lifetime than the singlet state.

As discussed in Sec. III B 2, in diF TES-ADT and diF TBDMS-ADT crystals, we assign the “fast” (sub-nanosecond) decay, which is only weakly temperature dependent (Table SII), to delocalized Frenkel excitons. This “fast” component primarily emits on the blue edge of the PL spectrum, and it is responsible for most of the total PL emission—55%–63% (67%–92%) for diF TES-ADT (diF TBDMS-ADT)—growing in relative weight with temperature, Fig. 10(a) [Fig. 10(b)]. The short lifetime of this component (more than an order of magnitude faster than that for isolated molecules in dilute solution,  $\tau_{FC} = 10$  ns) suggests that nonradiative decay pathways—including both scattering into the ground state and conversion into a different excited state—compete strongly with the radiative decay for this state. In diF TBDMS-ADT, the delocalized exciton behavior was well described in the framework of 1D J-aggregates, whereas in diF TES-ADT, the temperature dependence of  $N_{coh}$  was considerably weaker than that expected from either 1D or 2D aggregates<sup>2</sup> and delocalization was limited to  $\sim 2$  molecules at all temperatures as compared to 4–7 molecules in diF TBDMS-ADT, depending on the temperature.

The “intermediate” component (with lifetime  $1/k_2 = 3$  ns–5 ns) in diF TES-ADT and diF TBDMS-ADT crystals is attributed to the <sup>1</sup>(TT) state. In both crystals, the average rise time of this state was 0.64 ns–0.66 ns (Table SII), comparable to the lifetime of the delocalized Frenkel exciton. This suggests that <sup>1</sup>(TT) is populated via the Frenkel exciton. Ultrafast pump–probe measurements of the same systems suggest that other formation pathways are possible on

faster timescales, but they also confirm that <sup>1</sup>(TT) is formed directly from the singlet exciton.<sup>65</sup> The line shape of the “intermediate” component shows preferential emission at lower energies, and it has a vibronic structure with transition energies similar to the Frenkel (“fast”) component. At low temperatures, the 0-0 emission peak is very small [negligible for diF TES-ADT at  $T < 160$  K, Fig. 9(b)], but it increases with temperature with  $\sim 0.06$  eV activation energy, which we attribute to the energy barrier for “back-conversion” of the <sup>1</sup>(TT) state to the  $S_1$  state. This is consistent with previous observations in diF TES-ADT films.<sup>28</sup> The large activation energy of 0.12 eV obtained from Arrhenius fits of the <sup>1</sup>(TT) state lifetime [Eq. (4)] suggests that in diF TES-ADT crystals, this state is stabilized and does not readily convert into, for example, free triplet states ( $T_1$ ). In particular, since the latter would be a major decay channel for the <sup>1</sup>(TT) state, short <sup>1</sup>(TT) lifetimes and their activation energies on the order of thermal energy would be expected for an efficient conversion to  $T_1$  states, which was not observed here. Qualitatively similar processes occur in diF TBDMS-ADT crystals. However, the energy barrier for the “back-conversion” of the <sup>1</sup>(TT) to  $S_1$  is considerably smaller [so that 0-0 emission is observed even at 78 K, Fig. 8(c)] and the activation energy for the <sup>1</sup>(TT) state lifetime is only  $\sim 0.007$  eV (the “intermediate” decay in Table SII).

In contrast to the other two diF R-ADT derivatives where the “fast” and “intermediate” decay components have very different behaviors pointing to different origins, these components in diF TSBS-ADT crystals appear to have similar origins, which we assign to the Davydov pair of Frenkel excitons seen in the absorption spectra. The components’ common origin is confirmed by their relatively

similar lifetimes ( $\sim 3$  ns and  $\sim 9$  ns), similar temperature dependencies [with  $E_a$  of Eq. (4) of 0.029 eV and 0.032 eV, respectively, Table SII], and nearly identical line shapes—other than a slight energy shift—at low temperatures [Fig. 8(e)]. The Frenkel character of these components is evidenced by their preferential emission via the 0-0 transition (on the blue edge), their similar lifetime to that of dilute solution (10 ns), and their small Stokes shift of  $\sim 0.058$  eV compared with  $\sim 0.078$  eV ( $\sim 0.13$  eV) for diF TBDMS-ADT (diF TES-ADT). Since the Davydov splitting in diF TSBS-ADT is only 0.045 eV, some thermal occupation of the upper Davydov state is expected across the whole temperature range studied here (78 K–293 K), but this occupation should be small at lower temperatures. This comports with the observed weights of the “fast” and “intermediate” components: the lower energy component (“intermediate”) is dominant at low temperatures but decreases in relative weight compared to the higher energy component (“fast”) as the temperature rises [Figs. 8(e), 8(f), and 10(c)].

For all three crystalline systems, we assign the “slow” component to emission from STEs similar to the excimers found in solution. First, the lifetimes of this component ( $1/k_3 = 16$  ns–30 ns at 78 K, depending on the crystal structure) are all longer than the radiative lifetime of diF R-ADT molecules ( $\sim 14$  ns).<sup>36</sup> While this precludes a Frenkel origin for the “slow” component, these long lifetimes are consistent with the excimer lifetime in solution (25 ns–40 ns depending on the side group, see Sec. III A). Second, the low temperature line shapes [Figs. 8 and S20(c)] have a broad main emission peak that is redshifted with respect to both the Frenkel and <sup>1</sup>(TT) main emission peaks, pointing to a lower excited state energy. Furthermore, the width of this peak contrasts with the clear vibronic structure of the Frenkel [e.g., Fig. 9(a)] and <sup>1</sup>(TT) emission [e.g., Fig. 9(b)]. Additionally, as the temperature increases, the “slow” component’s main emission peak redshifts substantially [e.g.,  $\sim 0.1$  eV, Fig. S20(c)]. This is pronouncedly different behavior as compared to that of the “fast” and “intermediate” components, and it is consistent with a thermally activated relaxation into lower energy states. Finally, the “slow” component emission also has a small amount of emission on the blue-edge [e.g., Fig. S20(c)], which is likely due to a delayed fluorescence process similar to that seen for the back-conversion of the <sup>1</sup>(TT) emission to  $S_1$  discussed above. Altogether, these observations indicate that the “slow” components are consistent with the excimer state found in solution (Sec. III A).

### C. Exciton properties depending on molecular packing: Comparison with DFT predictions

The intermolecular interactions expected in each crystalline system were quantified using TD-DFT methods, as discussed in the [supplementary material](#), which established that diF TBDMS-ADT is expected to have the strongest interactions and diF TSBS-ADT is expected to have the weakest interactions. This agrees well with our experimental observations of various features of optical properties discussed in Sec. III B and points to the impact that the packing structure of each crystal has on its excited state properties.

TD-DFT predicts that diF TSBS-ADT (1D “sandwich-herringbone” packing structure) has the smallest total exciton coupling<sup>2,66</sup> ( $V$ ) of the three systems, Table SIV. This suggests that the

Frenkel excitons in the diF TSBS-ADT crystal would be relatively localized so that the optical properties of the crystal would have properties similar to those of isolated molecules. This is seen in the absorption spectra of diF TSBS-ADT crystals as a small solution-to-crystal spectral shift, relatively narrow absorption peaks, a small Davydov splitting, and an overall line shape that most closely resembles that of solution (Sec. III B 1). In the PL spectra and kinetics (Sec. III B 2), this manifests as a relatively small Stokes shift ( $\sim 0.058$  eV) and Frenkel exciton lifetimes that are relatively similar to that of isolated molecules (indicating that these states are too localized to efficiently access nonradiative decay pathways), in contrast to the other diF R-ADT derivatives under study.

The small total exciton coupling ( $V < 5$  meV for all dimers, Table SIV) in diF TSBS-ADT are likely caused by the large slip distance between intra-chain dimers, which has been shown<sup>35</sup> to sensitively impact the value of the  $V$ , and the large separation ( $d > 12$  Å) between inter-chain dimers. In addition to the small values of  $V$  in this system, diF TSBS-ADT is also approximately a 1D material so that each molecule has only two nearest neighbors [e.g., for molecule 2, pairs 1–2 and 2–3 in Figs. 2(c) and 2(d)]. These facts combine to afford only a small amount of total interaction between Frenkel exciton states in diF TSBS-ADT.

In contrast to small values of  $V$  for these intra-chain dimers, the electron ( $t_e$ ) and hole ( $t_h$ ) transfer integral dimers ( $|t_e| = 20$  meV–40 meV and  $|t_h| = 10$  meV–25 meV) are of a similar magnitude to those found in the other derivatives (Table SIV). This may enable nontrivial mixing of the Frenkel and CT excitons—despite a small Frenkel delocalization—which in the absorption spectra manifests in the polarization dependence of the higher energy peaks (e.g., peak 3 in Fig. 4), which show substantial absorption when aligned with the CT exciton TDM [theoretically  $156^\circ$  off the  $a$ -axis, see Fig. S22(b)], indicative of a high CT character of that state. In the PL spectra, the nonzero electron and hole transfer integrals, combined with small interaction energies  $V$ , enable the formation of the excimer-like STEs,<sup>23</sup> which constitute a substantial fraction ( $\sim 45\%$  at 78 K) of the total PL in these crystals.

In diF TES-ADT and diF TBDMS-ADT crystals, TD-DFT predicts much larger exciton couplings ( $V$ ) (Table SIV). For example, the highest value of  $V$  in diF TBDMS-ADT (which is a 1D system) is  $\lesssim 52$  meV (see the [supplementary material](#) for discussion of the upper bound), and it is obtained for dimer interactions along the columnar stack [ $a$ -axis, e.g., pair 1–3 in Fig. 2(e)]. In the diF TES-ADT (a 2D system),  $V = 22$  meV for the  $a$ -axis dimers [e.g., pairs 1–2 in Fig. 2(a)] and 20 meV for the  $b$ -axis dimers [e.g., pair 1–3 in Fig. 2(a)]. In both systems, these intermolecular couplings can be seen in the absorption spectra, with large solution-to-crystal shift, broadening of the peaks, and, in diF TBDMS-ADT, a large Davydov splitting (Sec. III B 1, Table I). In the PL kinetics, the large value of  $V$  manifests as a rapid sub-nanosecond decay rate for the Frenkel state, coupled with the weak temperature dependence of the nonradiative rates (Sec. III B 2). In terms of features of molecular packing, the much higher exciton interaction energies  $V$  in the diF TES-ADT and diF TBDMS-ADT crystals as compared to those in diF TSBS-ADT are obtained for different reasons. In the case of diF TBDMS-ADT, the larger interaction comes from the much smaller slip distance between molecules in a column that enables a much larger  $\pi$ – $\pi$  overlap. In the case of diF TES-ADT, the slip distance between molecules is not substantially smaller than that of diF TSBS-ADT, but the 2D

nature of diF TES-ADT provides more neighbors to each molecule, which compensates for the lower  $\pi$ - $\pi$  overlap.

Both diF TES-ADT and diF TBDMS-ADT also have relatively large electron and hole transfer integrals. While for diF TBDMS-ADT, the coupling and largest transfer integrals ( $V$ ,  $t_h$  and  $t_e$ ) are all coincident along the  $a$ -axis dimers [e.g., 1–3 in Fig. 2(e)], it is peculiar that the diF TES-ADT dimer along the  $a + b$ -axis, which has the largest hole transfer integral ( $|t_h| = 68$  meV for the dimers in the  $a + b$ -direction), is not the dimer with the largest total exciton coupling  $V$  (i.e., dimers along the  $a$ - and  $b$ -axes). Similar to the case of diF TSBS-ADT, we observed the formation of excimer-like STEs in diF TES-ADT and diF TBDMS-ADT, possibly connected to these large charge transfer integrals. However, unlike diF TSBS-ADT, the interplay of charge and total exciton coupling in these geometries leads to shorter lifetimes of the STE emission (Table SII) and considerably lower contribution to the overall PL (Fig. 10). In this way, larger total exciton coupling appears to prevent the formation of the STE states.

It is interesting to note that just as excitons (studied here) are considerably more localized in diF TSBS-ADT than in diF TES-ADT, the charge carriers (holes) (studied in previous publications<sup>29,42</sup>) are also more localized in diF TSBS-ADT than in diF TES-ADT. This is evidenced by the much higher conductivity in diF TES-ADT crystals (2D packing) against diF TSBS-ADT crystals (1D packing).<sup>29,42</sup> However, such a comparison between exciton and charge carrier characteristics is less straightforward when comparing those in diF TBDMS-ADT and diF TES-ADT. In particular, the charge transport in diF TBDMS-ADT crystals is considerably less efficient than that in diF TES-ADT crystals [with FET hole mobilities of  $0.07$  cm<sup>2</sup>/(V s) and  $20$  cm<sup>2</sup>/(V s), respectively],<sup>29,43</sup> and so, the lower charge carrier delocalization in diF TBDMS-ADT is not well correlated with the higher exciton delocalization in this crystal. It is known that dimensionality plays a considerable role in the charge transport so that the 2D molecular packing motifs such as “brickwork” and “herringbone” facilitate charge transport.<sup>1</sup> However, this is not necessarily the case for exciton dynamics, and so, different material design principles could be needed for applications relying on exciton characteristics.

While the Frenkel and STE states were observed in all three crystals, the <sup>1</sup>(TT) state, of importance to singlet fission-related applications such as photovoltaics,<sup>28,67</sup> was only present in diF TES-ADT and diF TBDMS-ADT, and not in diF TSBS-ADT. This is consistent with results from ultrafast spectroscopy of these crystals, in which polarization-dependent and probe wavelength-dependent pump-probe experiments explicitly probed conversion of  $S_1$  to the <sup>1</sup>(TT) state with a sub-picosecond time resolution.<sup>65</sup> Also important is that at room temperature, it appears that the molecular packing motif of diF TES-ADT is more conducive to the formation of the stable <sup>1</sup>(TT) state, as compared to diF TBDMS-ADT (which strongly favors formation of short-lived delocalized Frenkel exciton).

## V. CONCLUSIONS

In summary, we examined the nature and properties of excitons in functionalized fluorinated diF R-ADT crystals, depending on the molecular packing dictated by the side group, R. The band-edge states observed in the absorption and PL spectra were of the Frenkel type in all crystals, with their delocalization properties dependent

upon the crystal structure. The highest Frenkel exciton delocalization, manifested through both the optical absorption and PL properties, was observed in diF TBDMS-ADT crystals characterized by the 1D “twisted-columnar” molecular packing motif (due to its large  $\pi$ - $\pi$  overlap of adjacent molecules), followed by diF TES-ADT with the 2D “brickwork” packing (due to its large number of nearest neighbors). In contrast, Frenkel excitons in the diF TSBS-ADT crystals with 1D “sandwich-herringbone” packing were localized. At the same time, this packing motif was the most conducive to formation of excimer-like self-trapped excitons at all temperatures studied (78 K–293 K), likely due to its nontrivial intra-chain charge transfer integrals combined with vanishing total exciton couplings. This is in contrast to diF TBDMS-ADT, in which formation of self-trapped excitons was considerably inhibited, even at low temperatures, due to an interplay of both relatively large charge transfer integrals and total exciton couplings. The diF TES-ADT derivative is an intermediate between the other two derivatives, exhibiting some self-trapped exciton formation at temperatures below 280 K. The nontrivial charge transfer integrals in all crystals studied here also manifest in the mixed CT/Frenkel character of higher-energy absorptive states. In addition to these singlet and CT states, triplet states were also observed, namely, the <sup>1</sup>(TT) state, which is a precursor to the free triplets created via singlet fission upon excitation of a singlet state. These were observed in diF TBDMS-ADT and diF TES-ADT derivatives, but not in diF TSBS-ADT. More studies are needed to ascertain the connection between the formation and stabilization of this state and the underlying intermolecular interactions.

## SUPPLEMENTARY MATERIAL

See the [supplementary material](#) for additional spectral data, detailed fitting procedures, and DFT results.

## ACKNOWLEDGMENTS

We thank Professor B. Gibbons, Dr. S. Parkin, and Dr. L. Zakharov for the access to the XRD facilities and single-crystal XRD structure determination. This work was supported by the National Science Foundation (Grant Nos. DMR-1808258 and DMREF-1627428).

## DATA AVAILABILITY

The data that support the findings of this study are available from the corresponding author upon reasonable request.

## REFERENCES

- O. Ostroverkhova, *Chem. Rev.* **116**, 13279 (2016).
- N. J. Hestand and F. C. Spano, *Chem. Rev.* **118**, 7069 (2018).
- B. Pac and P. Petelenz, *ChemPhysChem* **15**, 2801 (2014).
- H. Yamagata, J. Norton, E. Hontz, Y. Olivier, D. Beljonne, J. L. Brédas, R. J. Silbey, and F. C. Spano, *J. Chem. Phys.* **134**, 204703 (2011).
- N. J. Hestand and F. C. Spano, *Acc. Chem. Res.* **50**, 341 (2017).
- A. Austin, N. J. Hestand, I. G. Mckendry, C. Zhong, X. Zhu, M. J. Zdilla, F. C. Spano, and J. M. Szarko, *J. Phys. Chem. Lett.* **8**, 1118 (2017).

- <sup>7</sup>R. D. Pensack, A. J. Tilley, S. R. Parkin, T. S. Lee, M. M. Payne, D. Gao, A. A. Jahnke, D. G. Oblinsky, P.-F. Li, J. E. Anthony *et al.*, *J. Am. Chem. Soc.* **137**, 6790 (2015).
- <sup>8</sup>K. Miyata, F. S. Conrad-Burton, F. L. Geyer, and X.-Y. Zhu, *Chem. Rev.* **119**, 4261 (2019).
- <sup>9</sup>Z. Guo, D. Lee, R. D. Schaller, X. Zuo, B. Lee, T. Luo, H. Gao, and L. Huang, *J. Am. Chem. Soc.* **136**, 10024 (2014).
- <sup>10</sup>H. Tamura and I. Burghardt, *J. Am. Chem. Soc.* **135**, 16364 (2013).
- <sup>11</sup>A. D. Poletayev, J. Clark, M. W. B. Wilson, A. Rao, Y. Makino, S. Hotta, and R. H. Friend, *Adv. Mater.* **26**, 919 (2014).
- <sup>12</sup>D. Beljonne, H. Yamagata, J. Brédas, F. C. Spano, and Y. Olivier, *Phys. Rev. Lett.* **110**, 226402 (2013).
- <sup>13</sup>E. Busby, T. C. Berkelbach, B. Kumar, A. Chernikov, Y. Zhong, H. Hlaing, X.-Y. Zhu, T. F. Heinz, M. S. Hybertsen, M. Y. Sfeir *et al.*, *J. Am. Chem. Soc.* **136**, 10654 (2014).
- <sup>14</sup>S. Tavazzi, L. Raimondo, L. Silvestri, P. Spearman, A. Camposeo, M. Polo, and D. Pisignano, *J. Chem. Phys.* **128**, 154709 (2008).
- <sup>15</sup>J. J. Burdett and C. J. Bardeen, *J. Am. Chem. Soc.* **134**, 8597 (2012).
- <sup>16</sup>P. M. Zimmerman, F. Bell, D. Casanova, and M. Head-Gordon, *J. Am. Chem. Soc.* **133**, 19944 (2011).
- <sup>17</sup>P. Irkhin, A. Rysanyanskiy, M. Koehler, and I. Biaggio, *Phys. Rev. B* **86**, 085143 (2012).
- <sup>18</sup>N. J. Hestand, H. Yamagata, B. Xu, D. Sun, Y. Zhong, A. R. Harutyunyan, G. Chen, H.-L. Dai, Y. Rao, and F. C. Spano, *J. Phys. Chem. C* **119**, 22137 (2015).
- <sup>19</sup>S. Tavazzi, A. Borghesi, A. Papagni, P. Spearman, L. Silvestri, A. Yassar, A. Camposeo, M. Polo, and D. Pisignano, *Phys. Rev. B* **75**, 245416 (2007).
- <sup>20</sup>P. Cudazzo, F. Sottile, A. Rubio, and M. Gatti, *J. Phys.: Condens. Matter* **27**, 113204 (2015).
- <sup>21</sup>C. Cocchi, T. Breuer, G. Witte, and C. Draxl, *Phys. Chem. Chem. Phys.* **20**, 29724 (2018).
- <sup>22</sup>C. Ramanan, A. L. Smeigh, J. E. Anthony, T. J. Marks, and M. R. Wasielewski, *J. Am. Chem. Soc.* **134**, 386 (2012).
- <sup>23</sup>G. B. Piland and C. J. Bardeen, *J. Phys. Chem. Lett.* **6**, 1841 (2015).
- <sup>24</sup>C. J. Bardeen, *Annu. Rev. Phys. Chem.* **65**, 127 (2014).
- <sup>25</sup>G. Akselrod, P. Deotare, N. Thompson, J. Lee, W. Tisdale, M. Baldo, V. Menon, and V. Bulović, *Nat. Commun.* **5**, 3646 (2014).
- <sup>26</sup>T. Rangel, A. Rinn, S. Sharifzadeh, F. H. da Jornada, A. Pick, S. G. Louie, G. Witte, L. Kronik, J. B. Neaton, and S. Chatterjee, *Proc. Natl. Acad. Sci. U. S. A.* **115**, 284 (2018).
- <sup>27</sup>A. M. Philip, S. K. Manikandan, A. Shaji, and M. Hariharan, *Chem.-Eur. J.* **24**, 18089 (2018).
- <sup>28</sup>C. Yong, A. Musser, S. Bayliss, S. Lukman, H. Tamura, O. Bubnova, R. Resel, M. Maruyama, S. Hotta, L. Herz *et al.*, *Nat. Commun.* **8**, 15953 (2017).
- <sup>29</sup>Z. Lampion, K. Barth, H. Lee, E. Gann, S. Engmann, H. Chen, M. Guthold, J. McCulloch, J. E. Anthony, L. Richter *et al.*, *Nat. Commun.* **9**, 5130 (2018).
- <sup>30</sup>M. Niazi, R. Li, E. Li, A. Kirmani, M. Abdelsamie, Q. Wang, W. Pan, M. Payne, J. E. Anthony, D. Smilgies *et al.*, *Nat. Commun.* **6**, 8598 (2015).
- <sup>31</sup>J. D. B. Van Schenck, E. K. Tanyi, L.-J. Cheng, J. Anthony, and O. Ostroverkhova, *MRS Commun.* **9**, 956 (2019).
- <sup>32</sup>M. Held, A. Graf, Y. Zakharko, P. Chao, L. Tropic, M. C. Gather, and J. Zaumseil, *Adv. Opt. Mater.* **6**, 1700962 (2018).
- <sup>33</sup>D. Polak, R. Jayaprakash, A. Leventis, K. Fallon, H. Coulthard, J. Anthony, P. Li, P. H. Bronstein, D. Lidzey *et al.*, *Chem. Sci.* **11**, 343 (2020).
- <sup>34</sup>D. Sanvitto and S. Kéna-Cohen, *Nat. Mater.* **15**, 1061 (2016).
- <sup>35</sup>A. Platt, M. Kendrick, M. Loth, J. Anthony, and O. Ostroverkhova, *Phys. Rev. B* **84**, 235209 (2011).
- <sup>36</sup>A. D. Platt, J. Day, S. Subramanian, J. E. Anthony, and O. Ostroverkhova, *J. Phys. Chem. C* **113**, 14006 (2009).
- <sup>37</sup>C. Y. Wong, B. D. Folie, B. L. Cotts, and N. S. Ginsberg, *J. Phys. Chem. Lett.* **6**, 3155 (2015).
- <sup>38</sup>W. E. B. Shepherd, A. D. Platt, M. J. Kendrick, M. A. Loth, J. E. Anthony, and O. Ostroverkhova, *J. Phys. Chem. Lett.* **2**, 362 (2011).
- <sup>39</sup>W. E. B. Shepherd, A. D. Platt, D. Hofer, O. Ostroverkhova, M. Loth, and J. E. Anthony, *Appl. Phys. Lett.* **97**, 163303 (2010).
- <sup>40</sup>O. Jurchescu, D. Mourey, S. Subramanian, S. Parkin, B. Vogel, J. Anthony, T. Jackson, and D. Gundlach, *Phys. Rev. B* **80**, 085201 (2009).
- <sup>41</sup>K. Paudel, G. Giesbers, J. Van Schenck, J. E. Anthony, and O. Ostroverkhova, *Org. Electron.* **67**, 311 (2019).
- <sup>42</sup>K. P. Goetz, Z. Li, J. W. Ward, C. Bougher, J. Rivnay, J. Smith, B. R. Conrad, S. R. Parkin, T. D. Anthopoulos, A. Salleo *et al.*, *Adv. Mater.* **23**, 3698 (2011).
- <sup>43</sup>B. Conrad, C. Chan, M. Loth, S. Parkin, X. Zhang, D. Delongchamp, J. Anthony, and D. Gundlach, *Appl. Phys. Lett.* **97**, 133306 (2010).
- <sup>44</sup>K. Paudel, B. Johnson, A. Neunzert, M. Thieme, B. Purushothaman, M. M. Payne, J. E. Anthony, and O. Ostroverkhova, *J. Phys. Chem. C* **117**, 24752 (2013).
- <sup>45</sup>R. J. Kline, S. D. Hudson, X. Zhang, D. J. Gundlach, A. J. Moad, O. D. Jurchescu, T. N. Jackson, S. Subramanian, J. E. Anthony, M. F. Toney *et al.*, *Chem. Mater.* **23**, 1194 (2011).
- <sup>46</sup>R. K. Hallani, K. J. Thorley, Y. Mei, S. R. Parkin, O. D. Jurchescu, and J. E. Anthony, *Adv. Funct. Mater.* **26**, 2341 (2016).
- <sup>47</sup>N. Shioya, R. Murdey, K. Nakao, H. Yoshida, T. Koganezawa, K. Eda, T. Shimoaka, and T. Hasegawa, *Sci. Rep.* **9**, 579 (2019).
- <sup>48</sup>P. Hall and B. Selinger, *J. Phys. Chem.* **85**, 2941 (1981).
- <sup>49</sup>M. Maus, M. Cotlet, J. Hofkens, T. Gensch, F. C. De Schryver, J. Schaffer, and C. A. M. Seidel, *Anal. Chem.* **73**, 2078 (2001).
- <sup>50</sup>S. Sharifzadeh, C. Y. Wong, H. Wu, B. L. Cotts, L. Kronik, N. S. Ginsberg, and J. B. Neaton, *Adv. Funct. Mater.* **25**, 2038 (2015).
- <sup>51</sup>R. L. Martin, *J. Chem. Phys.* **118**, 4775 (2003).
- <sup>52</sup>M. Frisch, G. Trucks, H. Schlegel, G. Scuseria, M. Robb, M. Cheeseman, G. Scalmani, V. Barone, G. Petersson, H. Nakatsuji *et al.*, Gaussian 16, Wallingford, CT, 2016.
- <sup>53</sup>H. Yamagata, D. S. Maxwell, J. Fan, K. R. Kittilstved, A. L. Briseno, M. D. Barnes, and F. C. Spano, *J. Phys. Chem. C* **118**, 28842 (2014).
- <sup>54</sup>J. D. B. Van Schenck, G. Giesbers, A. Kannegulla, L.-J. Cheng, J. E. Anthony, and O. Ostroverkhova, *MRS Adv.* **3**, 3465 (2018).
- <sup>55</sup>M. J. Kendrick, A. Neunzert, M. M. Payne, B. Purushothaman, B. D. Rose, J. E. Anthony, M. M. Haley, and O. Ostroverkhova, *J. Phys. Chem. C* **116**, 18108 (2012).
- <sup>56</sup>W. E. B. Shepherd, R. Grollman, A. Robertson, K. Paudel, R. Hallani, M. A. Loth, J. E. Anthony, and O. Ostroverkhova, *Chem. Phys. Lett.* **629**, 29 (2015).
- <sup>57</sup>J. C. Dean, R. Zhang, R. K. Hallani, R. D. Pensack, S. N. Sanders, D. G. Oblinsky, S. R. Parkin, J. E. Anthony, and G. D. Scholes, *Phys. Chem. Chem. Phys.* **19**, 23162 (2017).
- <sup>58</sup>Y. Liu, J. Silver, R.-J. Xie, J. Zhang, H. Xu, H. Shao, J. Jiang, and H. Jiang, *J. Mater. Chem. C* **5**, 12365 (2017).
- <sup>59</sup>H. L. Stern, A. J. Musser, S. Gelinias, P. Parkinson, L. M. Herz, M. J. Bruzek, J. Anthony, R. H. Friend, and B. J. Walker, *Proc. Natl. Acad. Sci. U. S. A.* **112**, 7656 (2015).
- <sup>60</sup>Z. Birech, M. Schwoerer, T. Schmeiler, J. Pflaum, and H. Schwoerer, *J. Chem. Phys.* **140**, 114501 (2014).
- <sup>61</sup>J. Lee, M. J. Bruzek, N. J. Thompson, M. Y. Sfeir, J. E. Anthony, and M. A. Baldo, *Adv. Mater.* **25**, 1445 (2013).
- <sup>62</sup>D. T. James, J. M. Frost, J. Wade, J. Nelson, and J.-S. Kim, *ACS Nano* **7**, 7983 (2013).
- <sup>63</sup>Y. Li, J. Wan, and D. Smilgies, *Phys. Rev. Res.* **2**, 033294 (2020).
- <sup>64</sup>T.-S. Ahn, A. M. Müller, R. O. Al-Kaysi, F. C. Spano, J. E. Norton, D. Beljonne, J.-L. Brédas, and C. J. Bardeen, *J. Chem. Phys.* **128**, 054505 (2008).
- <sup>65</sup>G. Mayonado, K. Vogt, J. Van Schenck, O. Ostroverkhova, and M. Graham, in *Ultrafast Phenomena*, 2020.
- <sup>66</sup>G. D. Scholes, R. D. Harcourt, and K. P. Ghiggino, *J. Chem. Phys.* **102**, 9574 (1995).
- <sup>67</sup>M. W. B. Wilson, A. Rao, B. Ehrler, and R. H. Friend, *Acc. Chem. Res.* **46**, 1330 (2013).